Comprehensive calculations of three–body breakup cross sections

E. Garrido

Instituto de Estructura de la Materia, CSIC, Serrano 123, E-28006 Madrid, Spain

D.V. Fedorov and A.S. Jensen

Institute of Physics and Astronomy, Aarhus University, DK-8000 Aarhus C, Denmark

We present in detail a theoretical model for fragmentation reactions of three–body halo nuclei. The different reaction mechanisms corresponding to the different processes are described and discussed. Coulomb and nuclear interactions are simultaneously included and the method is therefore applicable for any target, light, intermediate and heavy. Absolute values of many differential cross sections are then available as function of beam energy and target. We apply the method to fragmentation of ^{6}He and ^{11}Li on C, Cu and Pb. A large variety of observables, cross sections and momentum distributions, are computed. In almost all cases we obtain good agreement with the available experimental data.

PACS: 25.60.-t, 25.10.+s, 21.45.+v

1 Introduction

The peculiar structure of halo nuclei is clearly revealed by fragmentation reactions [1–4]. Large interaction cross sections and narrow momentum distributions of the fragments observed after fragmentation of these nuclei are direct signs of their large spatial extension. The main properties of these nuclei are well described by few–body models [5,6], where the nucleus is viewed as an inert core surrounded by a few (usually one or two) bound nucleons. Among them, Borromean two–neutron halo nuclei have attracted a lot of attention, and their most prominent examples, ^{6}He and ^{11}Li, have been widely investigated.

Preprint submitted to Elsevier Preprint *9 May 2001*

During the last decade a large amount of experimental data after fragmentation of ^{6}He and ^{11}Li on different targets have been provided. In particular total dissociation cross sections and total interaction cross sections, as well as momentum distribution of the fragments after dissociation and after core breakup are available [7–18]. Different models describing these data have been developed. These models fall in two independent main groups according to the kind of reaction for which they were designed. The first one considers nuclear breakup processes, and therefore they apply to the case of light targets. Most of them describe neutron dissociation reactions while core breakup is usually omitted [19,20]. Only calculations performed in the framework of the Glauber theory are also providing total interaction cross sections [21–23]. The second group focuses on heavy targets where only Coulomb dissociation is considered [24–27]. Intermediate targets where nuclear and Coulomb interaction compete is outside the scope of these models. At best Coulomb and nuclear breakup are computed in independent models and subsequently simply added [28,29].

The reaction mechanisms responsible for the breakup processes are still controversial [30–32], but absolutely essential to understand and analyze the data properly [33]. It is established that few-body aspects of the halos are necessary. In most investigations halo constituents (and targets) are treated as inert particles where the intrinsic degrees of freedom are neglected or accounted for by finite range potentials with Pauli forbidden states. However, the core degrees of freedom are unavoidable for some observables like interaction cross sections where core destruction is substantial. Such many-body aspects must be included at some point while maintaining the necessary halo features.

More than one reaction mechanism is necessary in a correct description of halo breakup. The long range Coulomb and the short range nuclear potentials already lead to clear-cut differences [30,31]. However the finite extension of halo particles and targets furthermore produces inevitable differences in the active reaction mechanisms at small and large impact parameters. This has strong implications for the understanding and the analyses.

The starting point for developing our model was the recognition that, for large beam energies ($\gtrsim$ 100 MeV/nucleon), the time scales allow application of the sudden approximation for two-neutron [34,35] and one-neutron halos [36]. Only light targets, relative momentum distributions and the specifically dominating processes were accessible within the sudden approximation. The next step was to use a participant-spectator separation and employ the phenomenological optical model to describe the interactions between participants and target [37]. Again only light targets were accessible but now absolute cross sections were computed. The model was then extended to treat the interactions between spectators and target in the black sphere model [20]. Finally the Coulomb and nuclear interactions were included on the same footing allowing treatment of light, intermediate and heavy targets and computation of absolute values of all differential breakup cross sections [30,31].

The reaction mechanisms now come out as clearly distinguishable for light and heavy targets or rather for small and large impact parameters. The small impact parameters involve violent collisions and one or more of the halo particles do not arrive in the detectors in the forward direction. At large impact parameters the momentum transfer is relatively small and the three halo particles are gently excited into the continuum state, which subsequently decays and all halo particles most likely arrive in the forward detectors. These two extremes are separated roughly at impact parameters slightly larger than corresponding to grazing collisions. These different reaction mechanisms imply that the two-step processes, where one halo particle is removed by the target while the resonance of the remaining system is populated followed by decay [14–18], at best only is consistent with small momentum transfer [33]. The large momentum transfer requires a completely different mechanism of halo particle removal.

In this paper we formulate for the first time in detail the model accounting for all these effects. So far no other model contains all the necessary features. The idea is to describe the fragmentation reaction as the sum of all the possible reactions where one, two or all three halo constituents interact simultaneously with the target. The processes leading to different final states clearly add up incoherently. The cross sections for the remaining processes are in all the numerical applications in this report also simply added as appropriate for large momentum transfer from the target. The model is consistently describing two–neutron halo fragmentation on any target with simultaneous treatment of nuclear and Coulomb interactions. Absolute values are computed for all possible dissociation cross sections distinguished according to the particles left in the final state. Two–neutron removal cross sections, core breakup cross sections, interaction cross sections and momentum distributions are computed as function of target and beam energy above 50 MeV/nucleon. We shall present results for a large variety of these observables arising from fragmentation reactions of ^{6}He and ^{11}Li on C, Cu, and Pb. These three targets have been chosen as typical examples for light, intermediate and heavy targets displaying different reaction mechanisms due to the interplay of Coulomb and nuclear interactions. Details of the model are given in Sections 2 and 3. Results for fragmentation reactions of ^{6}He and ^{11}Li on C, Cu and Pb are shown in Section 4. Finally Section 5 contains summary and conclusions.

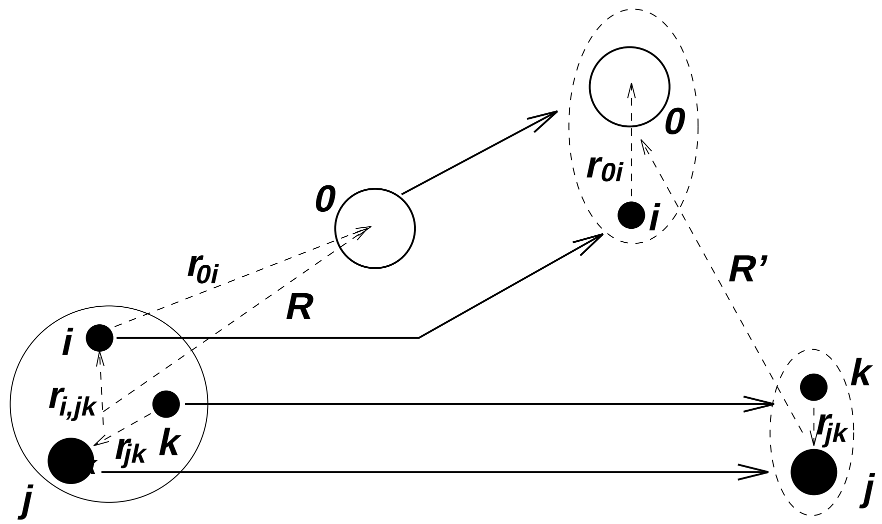

Fig. 1. Sketch of the reaction and coordinates used for the final state two by two separation. The target is labeled by 0 and $\{i, j, k\}$ label the particles within the three–body projectile.

2 Model and method for inert particles

We consider a spatially extended three–body halo nucleus colliding with a target at high energy. Let us first assume that the target and the three halo constituents in the projectile are inert particles. The differential cross section $d\sigma$ is to a good approximation given by the sum of three terms $d\sigma^{(i)}$, each of them describing the independent contribution to the process from the interaction between the target and the halo particle i. This is the assumption used in the classical formulation for a weakly bound projectile [38]. We neglect the binding energy of the initial three-body bound state compared to the high energy of the beam.

The reaction is then described as three particles independently interacting with the target as if each particle were free. Each individual interaction with the target is viewed as removal of one particle i (participant) while the other two particles j and k (spectators) both survive the reaction undisturbed (see Fig. 1). The participant is either absorbed (in the optical model sense) or elastically scattered (diffracted) by the target.

The masses, coordinates and conjugate momenta are denoted m, $\boldsymbol{r}$ and $\boldsymbol{p}$, respectively. The three halo particles and the target are labeled by $\{i, j, k\} = \{1, 2, 3\}$ and 0, respectively. The relative coordinates $\boldsymbol{r}_{jk}$, $\boldsymbol{r}_{0i}$, $\boldsymbol{r}_{i,jk}$, $\boldsymbol{R}$ and $\boldsymbol{R}'$ are defined as shown in Fig. 1. The corresponding conjugate momenta are analogously denoted by $\boldsymbol{p}_{jk}$, $\boldsymbol{p}_{0i}$, $\boldsymbol{p}_{i,jk}$, $\boldsymbol{P} \equiv \boldsymbol{p}_{0,ijk}$ and $\boldsymbol{P}' \equiv \boldsymbol{p}'_{0i,jk}$. We use primes to denote the momenta in the final state. Detailed expressions for the different relative coordinates and momenta can be found in [20]. The momentum transfer in the reaction for elastic scattering of the participant is then given by

$$\boldsymbol{q} = \boldsymbol{p}_0 - \boldsymbol{p}'_0 = \boldsymbol{p}_{0i} - \boldsymbol{p}'_{0i} \ \ , \ \ q \equiv |\boldsymbol{q}| = 2p_{0i} \sin\frac{\theta}{2} \ , \tag{1}$$

where θ is the angle between $\boldsymbol{p}_{0i}$ and $\boldsymbol{p}'_{0i}$.

2.1 Two by two separation in the final state

For relatively large momentum transfer between participant and target the final state is appropriately described as two independent subsystems, i.e. the target plus participant and the two spectators. This separation is not a matter of convenience but dictated by physics, especially in connection with the generalization in the next section to spatially extended particles. This is a central assumption reflecting the reaction mechanism. It is discussed in previous publications and tested by comparison with experimental results [12,14,16,17,33,34]. The transition amplitude of the process in Fig. 1 can then within the mixed plane/distorted wave Born approximation be written as [20,39]

$$T^{(i)} = \langle \phi^{(0i-)}_{\boldsymbol{p}'_{0i}\Sigma'_i} \phi^{(jk-)}_{\boldsymbol{p}'_{jk} s'_{jk} \Sigma'_{jk}} e^{i\boldsymbol{P}'\cdot\boldsymbol{R}'} |V_{0i}| \Psi^{(JM)} e^{i\boldsymbol{P}\cdot\boldsymbol{R}} \rangle \ , \tag{2}$$

where J and M are the total angular momentum of the projectile and its projection on the z–axis, s'_{jk} and Σ'_{jk} are the spin and its third component of the two–body system formed by particles j and k after the collision, s'_i and Σ'_i are the spin and projection quantum numbers of particle i (for convenience we assume a spin zero target), and $\phi^{(0i-)}_{\boldsymbol{p}'_{0i}\Sigma'_i}$ and $\phi^{(jk-)}_{\boldsymbol{p}'_{jk} s'_{jk} \Sigma'_{jk}}$ are the distorted wave functions of the two final two–body systems. We use plane waves $e^{i\boldsymbol{P}'\cdot\boldsymbol{R}'}$ and $e^{i\boldsymbol{P}\cdot\boldsymbol{R}}$ because these relative momenta are much higher and the plane wave approximation is suitable.

In the frame of the projectile ($\boldsymbol{p}_i + \boldsymbol{p}_j + \boldsymbol{p}_k = 0$), and assuming that the participant i has spin 0 or 1/2, the previous transition amplitude leads to the following differential diffraction cross section for the process in Fig. 1

$$\frac{d^9\sigma^{(i)}_{el}(\boldsymbol{P}', \boldsymbol{p}'_{jk}, \boldsymbol{q})}{d\boldsymbol{P}' d\boldsymbol{p}'_{jk} d\boldsymbol{q}} = \frac{d^3\sigma^{(0i)}_{el}(\boldsymbol{p}_{0i} \to \boldsymbol{p}'_{0i})}{d\boldsymbol{q}} \, \frac{P_{dis}(\boldsymbol{q})}{2J+1} \sum_{M s'_{jk} \Sigma'_{jk} \Sigma'_i} |M^{(JM)}_{s_{jk}\Sigma'_{jk}\Sigma'_i}|^2 \ , \tag{3}$$

$$M^{(JM)}_{s'_{jk}\Sigma'_{jk}\Sigma'_i} = \langle \phi^{(jk-)}_{\boldsymbol{p}'_{jk} s'_{jk}\Sigma'_{jk}} e^{i\boldsymbol{p}_{i,jk}\boldsymbol{r}_{i,jk}} \chi_{s'_i\Sigma'_i} | \Psi^{(JM)} \rangle \ . \tag{4}$$

Note that the final two–body wave function $\phi^{(0i-)}_{\boldsymbol{p}'_{0i}\Sigma'_i}$ is contained in the differential elastic cross section for the participant–target scattering $d^3\sigma^{(0i)}_{el}/d\boldsymbol{q}$. The two–body wave function $\phi^{(jk-)}_{\boldsymbol{p}'_{jk}s'_{jk}\Sigma'_{jk}}$ is computed as in [35] and the appropriate phase factor is included in the computation of the overlap matrix element. When the participant i in the sense of the optical model is absorbed by the target the corresponding differential absorption cross section factorizes as

$$\frac{d^6\sigma^{(i)}_{abs}(\boldsymbol{P}', \boldsymbol{p}'_{jk})}{d\boldsymbol{P}' d\boldsymbol{p}'_{jk}} = \sigma^{(0i)}_{abs}(p_{0i}) \, \frac{1}{2J+1} \sum_{M s'_{jk}\Sigma'_{jk}\Sigma'_i} |M^{(JM)}_{s_{jk}\Sigma'_{jk}\Sigma'_i}|^2 \ . \tag{5}$$

The final state wave function used in eq.(2) is not orthogonal to the initial wave function. This means that our final state contains a non-zero component of three–body bound state plus target, that represents elastic scattering of the halo nucleus as a whole, and has to be removed. This is done in eq.(3) by means of the function $P_{dis}(\boldsymbol{q})$, that is the probability of dissociation of the three–body halo system. For elastic scattering the final state wave function of the halo nucleus is $e^{i\boldsymbol{q}_{cm}\cdot\boldsymbol{r}_{i,jk}}\Psi^{(JM)}$, where $\boldsymbol{q}_{cm} = \boldsymbol{q}(m_j+m_k)/(m_i+m_j+m_k)$ is the momentum transfer into the participant–spectators relative motion described by the coordinate $\boldsymbol{r}_{i,jk}$. Therefore the probability of elastic scattering of the three–body projectile as a whole is given by the square of the overlap between the initial and final three–body wave functions. This implies that the probability of dissociation is given by [40]

$$P_{dis}(\boldsymbol{q}) = 1 - |\langle \Psi^{(JM)} | e^{i\boldsymbol{q}_{cm}\cdot\boldsymbol{r}_{i,jk}} | \Psi^{(JM)} \rangle|^2 \ , \tag{6}$$

which vanishes as $q^2 (\propto \boldsymbol{q}^2_{cm})$ for small values of the momentum transfer.

In eqs.(3) and (5) $d^3\sigma^{(0i)}_{el}/d\boldsymbol{q}$ and $\sigma^{(0i)}_{abs}$ are the differential elastic and absorption cross sections for the participant–target scattering, respectively [41]. We use a central participant–target nuclear potential $V_N(r)$, and assuming that the participant and the target have charges Z_i and Z_0, respectively, the participant–target interaction is

$$V_{0i}(r) = \frac{Z_0 Z_i \alpha}{r} + V_N(r) \ , \tag{7}$$

where $\alpha = e^2/\hbar c$ is the electromagnetic coupling constant.

The cross sections arising from the interaction V_{0i} in eq.(7) are obtained after integration of eqs.(5) and (3) when particle i is absorbed and elastically

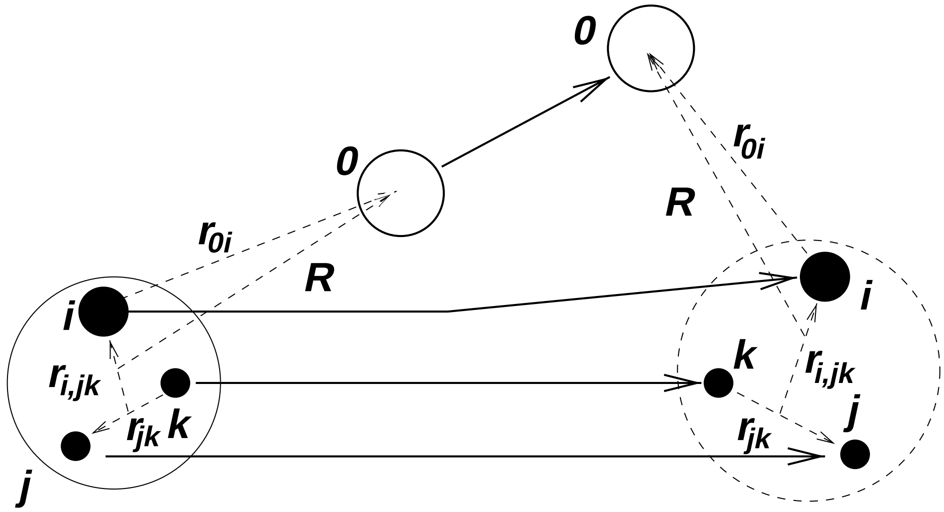

Fig. 2. Sketch of the reaction and coordinates used for the final state three by one separation. The notation is as in Fig. 1.

scattered, respectively.

2.2 Three by one separation in the final state

The scheme shown in Fig. 1 arises when the halo breakup is caused by a sufficiently violent and fast participant-target reaction. However this is not true in processes in which contributions from small momentum transfers are dominating. In these cases the small kick of the participant excites the halo rather gently and the breakup process proceeds via the created wave packet. An obvious example is halo breakup on a heavy target caused by the Coulomb participant–target interaction, which clearly is a dominating process, especially at low beam energies [30].

This type of gentle breakup reaction mechanism requires that the final state is that component of the three-body continuum halo wave function which at large distances approaches plane waves with relative momenta specified by $\boldsymbol{p}'_{jk}$ and $\boldsymbol{p}'_{i,jk}$. The corresponding reaction is sketched in Fig. 2. The transition matrix in eq.(2) should then be replaced by

$$T^{(i)} = \langle \Psi^{(-)}_{\mathbf{p}'_{jk}\mathbf{p}'_{i,jk}} \, \chi_{s'_i\Sigma'_i} \, \chi_{s'_{jk}\Sigma'_{jk}} \, e^{i\boldsymbol{P}'\cdot\boldsymbol{R}} | V_{0i}(r_{0i}) | \Psi^{(+)}_{\mathbf{P}}(R, \mathbf{r}_{jk}, \mathbf{r}_{i,jk}) \rangle \qquad (8)$$

where $\boldsymbol{R}$ now is the relative coordinate between the three–body system and the target, and $\boldsymbol{P}$ and $\boldsymbol{P}'$ are its conjugate momenta respectively in the initial and final state – note that in section 2.1 $\boldsymbol{P}'$ is the conjugate momentum of the relative radial coordinate between the center of mass of the two final two–body systems (see Fig. 1), while now $\boldsymbol{P}'$ is the conjugate momentum of the relative radial coordinate between the final three–body system and the target. The two spin wave functions χ are labeled by their respective final state total and projection quantum numbers $(s'_i\Sigma'_i)$ and $(s'_{jk}\Sigma'_{jk})$ defined earlier.

The distorted wave $\Psi^{(+)}_{\mathbf{P}}$ satisfies the equation

$$\left[-\frac{\hbar^2}{2M}\frac{\partial^2}{\partial\mathbf{R^2}}+V_{0i}(r_{0i})+H(\mathbf{r}_{jk},\mathbf{r}_{i,jk})-E\right]\Psi^{(+)}_{\mathbf{P}}=0, \tag{9}$$

where M is the projectile-target reduced mass and $H(\mathbf{r}_{jk},\mathbf{r}_{i,jk})$ is the intrinsic hamiltonian of the projectile. A gentle kick by a long range Coulomb potential implies that the halo absorbs the transfered momentum as a whole, meaning that the adiabatic approximation should be adequate for this reaction type.

We therefore as in [42] replace the intrinsic hamiltonian $H(\mathbf{r}_{jk},\mathbf{r}_{i,jk})$ with a constant, namely the ground state energy $-B$ of the halo. This ground state energy, typically a fraction of an MeV, is much smaller than the total energy E, typically of the order of hundred MeV, and can therefore be neglected. The internal coordinates $\mathbf{r}_{jk}$, $\mathbf{r}_{i,jk}$ are now no longer dynamical variables in the equation but parameters and therefore $d\mathbf{R}=d\mathbf{r}_{0i}$ leading to

$$\left[-\frac{\hbar^2}{2M}\frac{\partial^2}{\partial\mathbf{r}^2_{0i}}+V_{0i}(r_{0i})-E\right]\Psi^{(+)}_{\mathbf{P}}=0. \tag{10}$$

The solution to this equation is

$$\Psi^{(+)}_{\mathbf{P}}=\psi^{(+)}_{\mathbf{P}}(\,\mathbf{r}_{0i})\psi(\mathbf{r}_{jk},\mathbf{r}_{i,jk}), \tag{11}$$

where $\psi^{(+)}_{\mathbf{P}}(\,\mathbf{r}_{0i})$ is the distorted wave describing scattering of a particle with mass M in the potential V_{0i} and the function $\psi(\mathbf{r}_{jk},\mathbf{r}_{i,jk})$ is determined from the large $\mathbf{r}_{0i}$ asymptotics

$$\Psi^{(+)}_{\mathbf{P}}\stackrel{r_{0i}\to\infty}{\longrightarrow}\left(e^{i\mathbf{P}\mathbf{r}_{0i}}+f(\theta)\frac{e^{iPr_{0i}}}{r_{0i}}\right)\psi(\mathbf{r}_{jk},\mathbf{r}_{i,jk}). \tag{12}$$

Indeed, the plane-wave term of this expression describes a projectile in the ground state $\Psi^{(JM)}$ moving with the momentum P against the target, i.e.

$$e^{i\mathbf{P}\mathbf{r}_{0i}}\psi(\mathbf{r}_{jk},\mathbf{r}_{i,jk})=e^{i\mathbf{P}\cdot\mathbf{R}}\Psi^{(JM)}, \tag{13}$$

which gives

$$\psi(\mathbf{r}_{jk},\mathbf{r}_{i,jk})=e^{i\mathbf{P}\cdot\mathbf{R}-i\mathbf{P}\cdot\mathbf{r}_{0i}}\Psi^{(JM)}=e^{i\mu_i\mathbf{P}\cdot\mathbf{r}_{i,jk}}\Psi^{(JM)}, \tag{14}$$

where $\mu_i = (m_j + m_k)/(m_i + m_j + m_k)$. The matrix element $T^{(i)}$ in eq. (8) then becomes

$$
\begin{aligned}
T^{(i)} = & \langle \Psi^{(-)}_{\mathbf{p}'_{jk}\mathbf{p}'_{i,jk}} \; \chi_{s'_i\Sigma'_i} \; \chi_{s'_{jk}\Sigma'_{jk}} \; e^{i\mu_i \mathbf{P}'\cdot\mathbf{r}_{i,jk}} e^{i\mathbf{P}'\cdot\mathbf{r}_{0i}} | \\
& \times V_{0i}(r_{0i}) | \psi^{(+)}_{\mathbf{P}}(\mathbf{r}_{0i}) e^{i\mu_i \mathbf{P}\cdot\mathbf{r}_{i,jk}} \Psi^{(JM)} \rangle ,
\end{aligned}
\tag{15}
$$

which factorizes as

$$
\begin{aligned}
T^{(i)} = & \langle \Psi^{(-)}_{\mathbf{p}'_{jk}\mathbf{p}'_{i,jk}} \; \chi_{s'_i\Sigma'_i} \; \chi_{s'_{jk}\Sigma'_{jk}} \; | e^{i\mathbf{q}_{cm}\cdot\mathbf{r}_{i,jk}} | \Psi^{(JM)} \rangle \\
& \times \langle e^{i\mathbf{P}'\cdot\mathbf{r}_{0i}} | V_{0i}(r_{0i}) | \, \psi^{(+)}_{\mathbf{P}}(\mathbf{r}_{0i}) \rangle ,
\end{aligned}
\tag{16}
$$

where $\mathbf{q}_{cm} = \mu_i \mathbf{q}$ and $\mathbf{q} = \mathbf{P}' - \mathbf{P}$. The second factor is the matrix element $T^{(0i)}_{el}$ of the elastic scattering on the potential V_{0i} of a particle with mass M – that is the projectile-target scattering with the potential V_{0i}.

In addition to the breakup amplitude we obtain the elastic scattering of the halo as a whole simply by substituting the ground state wave function $\Psi^{(JM)}$ instead of the continuum wave function in the transition matrix element in eq.(8). This then leads to

$$
T^{(i)}_{el} = T^{(0i)}_{el} \; \langle \Psi^{(JM)} | e^{i\boldsymbol{q}_{cm}\cdot\boldsymbol{r}_{i,jk}} | \Psi^{(JM)} \rangle \; . \tag{17}
$$

For a two-neutron halo the largest contribution to the three-by-one final state is given at large impact parameters by the long-range Coulomb interaction between the charged core and the target. Considering only this main contribution we can write the breakup cross-section (with i designating the core) as

$$
\begin{aligned}
& \frac{d^9\sigma}{d\boldsymbol{P}' d\boldsymbol{p}'_{jk} d\boldsymbol{q}} = \frac{d^3\sigma^{(0p)}_{Ruth}}{d\boldsymbol{q}} \\
& \times \frac{1}{2J+1} \sum_{M,\Sigma'_i,s'_{jk},\Sigma'_{jk}} | \langle \Psi^{(-)}_{\boldsymbol{p}'_{jk},\boldsymbol{p}'_{i,jk}} \; \chi_{s'_i\Sigma'_i} \; \chi_{s'_{jk}\Sigma'_{jk}} \; | e^{i\boldsymbol{q}_{cm}\cdot\boldsymbol{r}_{i,jk}} | \Psi^{(JM)} \rangle |^2 \; ,
\end{aligned}
\tag{18}
$$

where the spin of the core is 0 or 1/2 and $d^3\sigma^{(0p)}_{Ruth}$ is simply the Rutherford projectile-target cross section.

When the two–body interactions between halo fragments in the final state are neglected in eq.(18) the matrix element simply reduces to the Fourier transform of the three-body bound state wave function with the momentum $\boldsymbol{p}_{i,jk}$ shifted by $\boldsymbol{q}_{cm}$.

2.2.1 The continuum three-body wave function

The three-body continuum wave function $\Psi^{(-)}_{\boldsymbol{p}'_{jk},\boldsymbol{p}'_{i,jk}}$ in eq.(18) has to be computed. We first introduce the Jacobi coordinates (see e.g. [5]) $\mathbf{x}$ and $\mathbf{y}$ and their conjugate momenta $\mathbf{k}_x$ and $\mathbf{k}_y$ such that $\mathbf{k}_x \cdot \mathbf{x} \equiv \boldsymbol{r}'_{jk} \cdot \boldsymbol{p}'_{jk}$ and $\mathbf{k}_y \cdot \mathbf{y} \equiv \boldsymbol{p}'_{i,jk} \cdot \boldsymbol{r}'_{i,jk}$. The corresponding hyperspherical coordinates ρ, Ω are then also available. We omit here the label i specifying which set of Jacobi coordinates. We then define the continuum three-body wave function $\Psi^{(-)}_{\mathbf{k}_x\mathbf{k}_y}(\mathbf{x},\mathbf{y})$ with the asymptotic behavior of a plane wave in six dimensions and an incoming hyperspherical wave

$$\Psi^{(-)}_{\mathbf{k}_x\mathbf{k}_y}(\mathbf{x},\mathbf{y}) \rightarrow \exp(i\mathbf{k}_x \cdot \mathbf{x} + i\mathbf{k}_y \cdot \mathbf{y}) + f^*(\Omega_\kappa, \Omega)\frac{\exp(-i\kappa\rho)}{\rho^{5/2}}, \qquad (19)$$

where we have introduced the 6-momentum $\kappa \equiv \{\mathbf{k}_x, \mathbf{k}_y\}$ and the corresponding hyperangular variables $\kappa = \sqrt{k_x^2 + k_y^2}$ and Ω_κ. The total energy is then given by κ as $E = \hbar^2\kappa^2/(2m)$.

We shall now express the function $\Psi_{\mathbf{k}_x\mathbf{k}_y}$ in terms of our adiabatic hyperspherical basis functions $\Phi_{JMn}(\rho,\Omega)$, see e.g.[6,34,43]. The basis functions Φ_{JMn} are labeled according to their asymptotic behavior, which means approaching the corresponding hyperspheric harmonics, i.e. $\Phi_{JMn}(\rho,\Omega) \rightarrow \mathbf{Y}_Q(\Omega)$ for large ρ. Here we use the notation $\mathbf{Y}_Q(\Omega)$ for a hyperspheric harmonic coupled with the appropriate spin functions to the total angular momentum, where $Q \equiv \{K, l_x, l_y, L, s_x, s_y, S, J, M\}$ denotes the full set of hyperradial quantum numbers, where $s_x = s_{jk}$ and $s_y = s_i$.

We now first shift the dependence of the function upon the five hyperangles Ω_κ of the momentum κ into the basis $Y_\xi(\Omega_\kappa)$ ($\xi \equiv \{K, l_x, l_y, L\}$) of the ordinary non-spin coupled hyperspheric harmonic. Thus we get

$$\Psi^{(-)}_{\mathbf{k}_x\mathbf{k}_y}(\mathbf{x},\mathbf{y})\ \chi_{s'_i\Sigma'_i}\ \chi_{s'_{jk}\Sigma'_{jk}} = \left[\sum_\xi \psi_\xi(\mathbf{x},\mathbf{y}) Y^*_\xi(\Omega_\kappa)\right] \chi_{s'_i\Sigma'_i}\ \chi_{s'_{jk}\Sigma'_{jk}}\ , \qquad (20)$$

where the function $\psi_\xi(\mathbf{x},\mathbf{y})$ now can be expanded in terms of our complete set of angular solutions $\Phi_{JMn}(\rho,\Omega)$ to the Faddeev equations i.e.

$$\psi_\xi(\mathbf{x},\mathbf{y})\chi_{s'_i\Sigma'_i}\ \chi_{s'_{jk}\Sigma'_{jk}} = \rho^{-5/2}\sum_{JMn} F^{(q)}_{JMn}(\rho)\Phi_{JMn}(\rho,\Omega)\ , \qquad (21)$$

where $q \equiv \{\xi, s'_{jk}, \Sigma'_{jk}, s'_i, \Sigma'_i\}$ is the set of quantum numbers equivalent to Q in the decoupled spin basis.

Inserting expansion eq.(21) into the Schrödinger equation we obtain, after multiplication by $\langle \Phi_{JMn}(\rho,\Omega)|$ and subsequent angular integration, our usual hyperradial equations for $F^{(q)}_{JMn}(\rho)$ [6,34,43]

$$\left(-\frac{\partial^2}{\partial\rho^2} + \frac{\lambda_n(\rho)+\frac{15}{4}}{\rho^2} + Q_{nn} - \frac{\hbar^2\kappa^2}{2m}\right) F^{(q)}_{JMn}(\rho)$$
$$= \sum_{n'\neq n}\left(-2P_{nn'}\frac{\partial}{\partial\rho} - Q_{nn'}\right) F^{(q)}_{JMn'}(\rho). \tag{22}$$

The asymptotic form eq.(19) can be expanded in terms of the hyperspheric harmonics $Y_\xi(\Omega_\kappa)$ using

$$\exp(i\mathbf{k}_x\mathbf{x} + i\mathbf{k}_y\mathbf{y}) = \frac{(2\pi)^3}{(\kappa\rho)^2}\sum_\xi i^K J_{K+2}(\kappa\rho) Y^*_\xi(\Omega_\kappa) Y_\xi(\Omega) \ , \tag{23}$$

which implies the asymptotic behavior

$$\Psi^{(-)}_{\mathbf{k}_x\mathbf{k}_y}(\mathbf{x},\mathbf{y}) \to \sum_{\xi\xi'}\Bigg(\delta_{\xi\xi'}\frac{(2\pi)^3\ i^K}{(\kappa\rho)^2} J_{K+2}(\kappa\rho)$$
$$+ f^*_{\xi\xi'}\frac{\exp(-i\kappa\rho)}{\rho^{5/2}}\Bigg) Y_{\xi'}(\Omega) Y^*_\xi(\Omega_\kappa) \ , \tag{24}$$

Then the asymptotic boundary condition for the hyperradial function $F^{(q)}_{JMn}(\rho)$ is found from eq.(24)

$$\rho^{-5/2} F^{(q')}_{JMn}(\rho) \to \sum_\xi \left[\frac{(2\pi)^3\ i^K}{(\kappa\rho)^2} J_{K+2}(\kappa\rho)\delta_{\xi\xi'} + f^*_{\xi\xi'}\frac{\exp(-i\kappa\rho)}{\rho^{5/2}}\right]$$
$$\times\langle \mathbf{Y}_Q | Y_\xi \chi_{s'_i\Sigma'_i}\ \chi_{s'_{jk}\Sigma'_{jk}}\rangle \ . \tag{25}$$

This boundary condition is equivalent to the scattering boundary condition used in [27].

The transition matrix element in eq.(18) reduces when $\boldsymbol{q}_{cm}\cdot\boldsymbol{r}_{i,jk} \ll 1$ to

$$i\boldsymbol{q}_{cm}\cdot\langle \Psi_{\boldsymbol{p}'_{jk},\boldsymbol{p}'_{i,jk}}\ \chi_{s'_i\Sigma'_i}\ \chi_{s'_{jk}\Sigma'_{jk}}\ |\boldsymbol{r}_{i,jk}|\Psi^{(JM)}\rangle \ , \tag{26}$$

which after squaring and summation over magnetic quantum numbers gives the usual factorized expression in terms of the $B(E1)$ dipole strength function and the cross section [27]. Before expansion this matrix element also included all the higher multipole transitions. They could in principle arise from the nuclear as well as the Coulomb interaction.

When the participant is charged the elastic cross section eq.(18) for $q \to 0$ is dominated by the Coulomb cross section, which after integration over the directions of $\boldsymbol{q}$ diverges like q^{-3}. Since the square of the matrix element in eq.(18) vanishes as q^2 for small q, the integration of eq.(18) over q leads to a logarithmic divergence of this elastic cross section. However, to produce dissociation, the energy transferred from target to participant ($\delta E \equiv \sqrt{\boldsymbol{p}_0^2 + m_0^2} - \sqrt{\boldsymbol{p}_0'^2 + m_0^2}$) must be larger than the three–body binding energy B. When $\boldsymbol{p}_0$ and $\boldsymbol{q} = \boldsymbol{p}_0 - \boldsymbol{p}_0'$ are parallel δE is maximized. For small B compared to the target rest mass $\delta E = B$ implies that $qc \approx q_L c \equiv B\sqrt{1 + m_0^2 c^2 / p_0^2}$, which reduces to B/v in the non–relativistic limit. Thus q must be larger than q_L to produce dissociation.

Another formal divergence arises for the Coulomb interaction at large impact parameters (low momentum transfer), where adiabatic motion only allows virtual excitations excluding dissociation. If the collision time Δt is long compared to the orbital period of motion T inside the projectile no transfer of energy occurs. These processes are excluded by the adiabatic cutoff. The decisive parameter is [44]

$$\xi_a \equiv \frac{\hbar \omega_a b}{\gamma \beta \hbar c} \,, \tag{27}$$

where $\beta = v/c$, $\gamma = (1 - \beta^2)^{-1/2}$ and $\hbar\omega_a$ is the adiabatic cutoff energy, i.e. the maximum value of the equivalent photon energy for a given impact parameter b estimated in a sharp cutoff model [44]. Then $\hbar\omega_a \approx B$, where B is the three-body binding energy, should be a reasonable estimate as the lowest energy needed for breakup. However, the softness of the electromagnetic excitation modes could influence this sharp cutoff value, but the effect on the cross sections is still only logarithmic. We leave the precise choice of $\hbar\omega_a$ for adjustments in the numerical computations.

In previous publications [30,31] we used $\hbar\omega_a = B_{ps}/\pi$, where B_{ps} is the binding energy between participant and the system consisting of the two spectators, i.e., $B_{ps} = B - B_{2s}$, where B_{2s} is the two–body binding energy of the two spectators. In a Borromean system B_{2s} is negative. This is a misleading connection for a slow reaction where the full projectile is adiabatically excited.

From [45] the following classical relation between the momentum transfer q and the impact parameter b is derived:

$$q = \frac{Z_i Z_0 e^2}{b} \frac{p}{E_{kin}} \,, \tag{28}$$

where p is the momentum of the projectile and E_{kin} its kinetic energy.

The adiabatic cutoff condition $\xi_a = 1$ and use of eqs.(27) and (28) leads then to $q > q_a$, where

$$q_a = \frac{Z_0 Z_i e^2}{(\hbar c)^2} \frac{\hbar \omega_a}{\gamma - 1} \; . \tag{29}$$

Therefore integration of eq.(18) has to include only values of the momentum transfer q larger than the largest of q_L and q_a. The divergence then disappears.

3 Model and method for spatially extended particles

The two different final state divisions described in Section 2 are introduced for physics reasons and not for convenience. The underlying idea is that dominating reaction contributions arise from (optical model type of) absorption, which implies that the final state consists of the spectators and the participant-target system, and elastic core-target Coulomb scattering at low momentum transfer leading to a final state containing all three halo particles. This division is dictated by the reaction mechanism and seems to be unavoidable in a few-body treatment where the core degrees of freedom are neglected. Furthermore, the finite extension of the projectile constituents and the target also requires a similar division according to the number of projectile constituents simultaneously colliding with the target.

3.1 Reaction scenarios

Let us extend the applicability of the inert particle model and incorporate effects of the core degrees of freedom and the finite sizes of the constituents. First we assume short–range interactions between each of the halo constituents and the target. Then we start by describing the individual constituent–target interaction in the black disk model, according to which the target absorbs the constituent inside a cylinder with the axis along the beam direction and otherwise leaves untouched. The radius of this cylinder is related to the range of the interaction and approximately equal to the sum of target and constituent radii. For the collision between the halo nucleus and the target we have then the four possibilities shown in Fig. 3:

(a) Only one of the halo constituents, the participant, is inside its cylinder. The other two constituents are mere spectators, and survive untouched after the

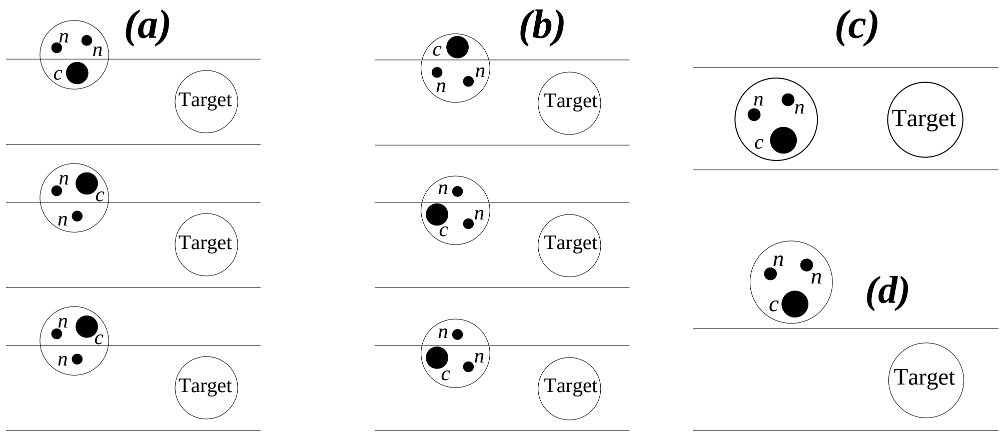

Fig. 3. Scheme of the possible scenarios for the collision between the three–body projectile and the target. The notation indicates a halo consisting of two neutrons and a core.

collision. The three constituents of the halo projectile give rise to three contributions of this kind.

(b) Two of the halo constituents are participants. The third one is spectator. Again we have three possible reactions of this kind.

(c) All the three halo constituents are inside their corresponding cylinders.

(d) All the three halo constituents are outside their cylinders. For short–range interactions this means that the whole projectile is untouched by the target, and this process would only contribute to the elastic cross section.

The scheme in Fig. 3 is only directly valid for short-range interactions and therefore not applicable for charged halos. This is a severe deficiency as even a two–neutron halo nucleus colliding with a heavy target involves a core-target Coulomb interaction that by far can dominate the cross section.

To incorporate long–range interactions into the model we do the following: In the reactions shown in Figs. 3a, 3b, and 3c the participant–target interaction contains two parts, the full short–range interaction and the long–range potential related to small impact parameters (large momentum transfer). The large impact parameter part of the long–range potentials (small momentum transfer) corresponds to reactions as the one shown in Fig. 3d.

In the particular case of two–neutron halo fragmentation this means that the momentum transfer between target and core is divided into large and small values corresponding to short and long impact parameters, respectively. Large momentum transfer contributions to the cross sections correspond to the processes shown in Figs. 3a, 3b, and 3c. They contain the nuclear core-target interaction and the large momentum transfer part of the Coulomb core–target interaction. They are described in Section 2.1, and the integral of eq.(3) over the momentum transfer involves values of q larger than a certain value q_g ($q_g < q < \infty$). Low momentum transfer contributions correspond to the process shown in Fig. 3d, where none of the halo constituents are inside their cylinders, and only the core-target Coulomb interaction contributes. Cross sections are obtained after integration of eq.(18), where the momentum transfer varies between $q_{min} = \max\{q_L, q_a\}$ and q_g.

Low and large impact parameters are divided by the value $b_g = R_0 + R_c + \pi a/2$, see [44], where R_0 and R_c are charge root mean square radii of the target and the core, and $a = \hbar c Z_0 Z_c e^2/2E_{kin}$ is half the distance of closest core-target approach. Use of eq.(28) and the fact that $p/E_{kin} = (\gamma+1)/\gamma\beta c$ then leads to the value q_g of the momentum separating low ($q < q_g$, $b > b_g$) and large momentum transfer ($q > q_g$, $b < b_g$), i.e.

$$q_g = \frac{\hbar Z_0 Z_c e^2}{b_g} \frac{\gamma+1}{\gamma\beta} \ . \tag{30}$$

3.2 Cross sections

According to the number of particles surviving in the final state we have the possible cross sections: σ_0, σ_n, σ_c, σ_{nn}, σ_{nc} and σ_{nnc}, where σ_0 means no particles in the final state, and the indexes c and n refer to the core and the neutrons surviving in the final state. If some of the particles are absent in the final state they have been absorbed by the target in the optical model sense.

The probabilities for finding the core and one halo neutron inside their cylinders are denoted P_c and P_n, respectively. These probabilities can be split in two parts, the probability of being absorbed by the target and the probability of being elastically scattered by the target: $P_c = P_c^{ab} + P_c^{el}$ and $P_n = P_n^{ab} + P_n^{el}$.

When the three–body halo projectile collides with the target, each of the reactions shown in Fig. 3a occur with the probability $P_i(1-P_j)(1-P_k)$, where the index i refers to the participant. In the same way each of the reactions shown in Fig. 3b and Fig. 3c occur with the probabilities $P_iP_j(1-P_k)$ and $P_iP_jP_k$. In this way, the total probability of a given process is obtained by adding the probabilities of all the processes in Fig. 3 producing precisely the corresponding group of halo constituents in the final state.

For instance, the probability of a process in which only the core survives in the final state (processes giving rise to σ_c) contains two terms, $P_n^{ab}P_n^{ab}(1-P_c)$, that comes from one of the reactions shown in Fig. 3b in which the two neutrons inside their cylinders are absorbed by the target, and $P_c^{el}P_n^{ab}P_n^{ab}$, that comes from the reaction shown in Fig. 3c in which the two halo neutrons are

Table 1
Contributions to the different cross sections from the reactions shown in Figs. 3a, 3b and 3c, where the nuclear interaction between the halo constituents plus the large momentum transfer (low impact parameter) part of the Coulomb core–target interactions are included. Two crosses mean that the contribution must be included twice due to the possible exchange of the two halo neutrons. The cross section σ_{nnc} contains also the contribution from the low momentum transfer (large impact parameter) part of the Coulomb core–target interaction sketched in Fig. 3d.

Reaction	Probability	σ_0	σ_n	σ_c	σ_{nn}	σ_{nc}	σ_{nnc}
Fig.3a	$P_c^{el}(1-P_n)(1-P_n)$						X
	$P_c^{ab}(1-P_n)(1-P_n)$				X		
	$P_n^{el}(1-P_n)(1-P_c)$						XX
	$P_n^{ab}(1-P_n)(1-P_c)$					XX	
Fig.3b	$P_c^{el}P_n^{el}(1-P_n)$						XX
	$P_c^{el}P_n^{ab}(1-P_n)$					XX	
	$P_c^{ab}P_n^{el}(1-P_n)$				XX		
	$P_c^{ab}P_n^{ab}(1-P_n)$		XX				
	$P_n^{el}P_n^{el}(1-P_c)$						X
	$P_n^{el}P_n^{ab}(1-P_c)$					XX	
	$P_n^{ab}P_n^{ab}(1-P_c)$			X			
Fig.3c	$P_c^{el}P_n^{el}P_n^{el}$						X
	$P_c^{el}P_n^{el}P_n^{ab}$					XX	
	$P_c^{el}P_n^{ab}P_n^{ab}$			X			
	$P_c^{ab}P_n^{el}P_n^{el}$				X		
	$P_c^{ab}P_n^{el}P_n^{ab}$		XX				
	$P_c^{ab}P_n^{ab}P_n^{ab}$	X					

absorbed and the core is scattered.

In Table 1 we indicate which reactions in Fig. 3 contribute to the various cross sections. The projectile contains two neutrons and some of the reactions should be counted twice, since the symmetric combination also contributes the same amount. The probabilities shown in Table 1 are not explicitly computed. Instead we compute the cross sections corresponding to each of the different processes. For example to compute the first process in Table 1 (Fig. 3a) we note that P_c^{el} corresponds to the probability for elastic scattering of the core on the target with the related cross section given by eq.(3). The constraints that the two neutrons must be outside the cylinders are imposed by removing appropriate parts of the initial three-body wave function, see section 4.2. All other processes in Fig. 3a are analogously computed by replacing the first probability by the related cross section and removing parts of the three-body wave function in the overlap in eq.(4) to account for the other probability factors, see section 4.2. When the probability factors appear symmetrically as for processes corresponding to Figs.3b and 3c a specific choice must be made. The details for each of the possible cases are described in sections 3.3, 3.4 and 3.5.

Differential cross sections are given in eqs.(3) and (5), and total cross sections are obtained after integration over all the variables. The cross section for a process in which a certain group of constituents survive in the final state is then computed by summation of the partial cross sections obtained from each of the contributing reactions shown in Table 1. We emphasize that on top of the contributions in the last column of Table 1 the cross section σ_{nnc} also contains the low momentum transfer part due to the Coulomb interaction that corresponds to the process in Fig. 3d.

From the cross sections σ_0, σ_n, σ_c, σ_{nn}, σ_{nc} and σ_{nnc} it is easy to obtain several cross sections of specific interest, as the two neutron removal cross section (σ_{-2n}), that is given by all the processes where the core survives in the final state; the core removal cross section (σ_{-c}), given by all the processes in which the core is destroyed by the target; and the interaction cross section (σ_I), defined as the cross section given by the reactions where the projectile looses at least one of its constituents:

$$\sigma_{-2n} = \sigma_c + \sigma_{nc} + \sigma_{nnc} \; , \; \sigma_{-c} = \sigma_0 + \sigma_n + \sigma_{nn} \; , \; \sigma_I = \sigma_{-2n} + \sigma_{-c} \; . \tag{31}$$

Adding the probabilities shown in Table 1 contributing to each of the cross sections we obtain the probabilities for the two–neutron removal and core breakup processes as

$$P(\sigma_{-2n}) = P_c^{el} + P_n(1 - P_c) + P_n(1 - P_n)(1 - P_c) \; , \tag{32}$$
$$P(\sigma_{-c}) = P_c^{ab} \; . \tag{33}$$

Therefore the cross sections σ_{-2n} and σ_{-c} can be computed as indicated in eq.(31), or, alternatively, by computing the cross sections corresponding to the probabilities in eqs.(32) and (33).

From eq.(32) we see that the two neutron removal cross section has three contributions. The first one, cross section corresponding to P_c^{el}, is the elastic scattering of the core by the target, and its differential cross section is given by eq.(3). Since P_c^{el} is the probability for the core being inside the cylinder, only large momentum transfer, $q > q_g$, should be included in eq.(3).

However, the two–neutron removal cross section also receives a contribution from the reaction in Fig. 3d, which contains the low momentum transfer part ($q_{min} < q < q_g$) of the core–target interaction. Thus, q is actually only restricted by $q > q_{min}$. In addition σ_{-2n} also contains the contribution from the strong interaction between the halo neutrons and the target with the core as spectator. These contributions are given by the cross sections corresponding to the second and third terms in eq.(32). They are computed from eqs.(3) and (5) with the corresponding optical model neutron-target cross section with the overlap in eq.(4) containing the appropriate parts of the three-body wave function. Core breakup cross sections can be computed, according to eq.(33), by considering only the core–target potential and subsequent integration of eq.(5).

3.3 Two–spectators contributions (Fig. 3a)

The contributions in Fig. 3a correspond to processes in which one halo constituent (participant) interacts with the target, while the other two (spectators) remain untouched. They contribute to the cross sections σ_{nn}, σ_{nc} and σ_{nnc} as shown in the upper part of Table 1. The general form for the probability of these reactions is $P_i(1 - P_j)(1 - P_k)$, where P_i is the probability for the halo constituent i being the participant.

The procedure is then as discussed in Section 3.2. The participant–target interaction is described by the potential eq.(7) where the nuclear part is given by an optical potential, that takes into account both absorption and elastic scattering of the participant by the target. The differential cross sections are given by eqs.(3) and (5), and total cross sections are obtained after integration over all the variables. These integrations must take into account the fact that impact parameters for constituents j and k are larger than the radii of their cylinders. This is done (see section 4.2) by removing the appropriate part of the three–body wave function in eq.(4).

When the core is participant the interference between Coulomb and nuclear core–target interactions is included in the calculation through the differential elastic participant–target cross section in eq.(3). It is important to keep in mind that the momentum transfer q in eq.(3) must be larger than q_g in eq.(30). This restriction includes only the low impact parameter part of the Coulomb interaction and allows therefore precisely the processes in question.

3.4 One–spectator contributions (Fig. 3b)

The contributions shown in Fig. 3b correspond to processes in which two of the halo constituents are inside their cylinders, while the third one is spectator. In principle each of the two participant constituents could be either absorbed or scattered by the target, and therefore the reactions shown in Fig. 3b can contribute to the cross sections σ_n, σ_c, σ_{nn}, σ_{nc} and σ_{nnc} as seen in the central part of Table 1.

The probability for occurrence of one of the reactions in Fig. 3b is $P_i P_j(1-P_k)$, where i and j refer to the two participants. To compute the cross section corresponding to this reaction we first select the constituent i or j where the interaction with the target is most conveniently described by the optical model. If possible we choose the core. Then the Coulomb interaction with the target and the interference between nuclear and Coulomb interactions are treated carefully.

Cross sections are then computed as a process in which one of the participants (i) interacts with the target through the corresponding optical potential. Differential cross sections are then given by eqs.(3) and (5) for elastic scattering and absorption of constituent i by the target. Again total cross sections are computed after integration of (3) and (5) over all the variables. When the core is participant only the low impact parameter part of the Coulomb interaction is allowed, and $q > q_g$ in eq.(3).

In this case (reactions in Fig. 3b) there is a second constituent, constituent j, inside its cylinder that therefore also interacts with the target. This fact is included in the calculations by removing the appropriate part of the three–body wave function in eq.(4), see sect.4.2. We then ensure that constituent j is close enough to the target to interact with it. As a result of this interaction constituent j can be either scattered or absorbed by the target. We then divide each of the cross sections computed as described above from eqs.(3) and (5) in two parts, one of them corresponding to absorption of constituent j by the target and the other one corresponding to scattering of constituent j. The weight of each of these parts can be obtained in the optical model for two–body systems, i.e. simply as $\sigma_{abs}^{(j)}/(\sigma_{abs}^{(j)}+\sigma_{ela}^{(j)})$ for absorption and $\sigma_{ela}^{(j)}/(\sigma_{abs}^{(j)}+\sigma_{ela}^{(j)})$ for scattering of constituent j. Here $\sigma_{abs}^{(j)}$ and $\sigma_{ela}^{(j)}$ are the absorption and elastic cross sections obtained by use of an optical potential describing the interaction between constituent j and the target.

Finally, an additional requirement is needed when computing cross sections. This is due to the fact that particle k is outside its cylinder, and therefore not interacting with the target. This is again included in the calculation by removing the appropriate part of the three–body wave function in eq.(4)

as described in section 4.2.

The procedure for constituents i, j and k described above permits to calculate cross sections for all the processes in Fig. 3b. It also permits to compute separately cross sections for processes where both, constituents i and j, are either absorbed or scattered, and also when one of them is scattered and the other one absorbed.

3.5 Zero–spectators contribution (Fig. 3c)

The contributions shown in Fig. 3c correspond to processes where all three constituents are inside the corresponding cylinders. The probability for this reaction is $P_i P_j P_k$, and any of the three constituents can be either absorbed or scattered by the target. Thus, this reaction contributes to cross sections where zero, one, two, or three constituents survive in the final state, as shown in the lower part of Table 1.

In analogy to the reactions in Fig. 3b we describe the core–target interaction with an optical nuclear potential plus the Coulomb interaction eq.(7). We then compute cross sections from eqs.(3) and (5) as a process in which the interaction between projectile and target takes place through the core–target potential. Once more, only the low impact parameter part of the Coulomb interaction is allowed, and $q > q_g$ in eq.(3).

Now, reactions in Fig. 3c, constituents j and k are also inside their cylinders, and therefore both interact with the target. As before, this is ensured by including in the overlap in eq.(4) the appropriate part of the three–body wave function (see sect.4.2). Again these two constituents can be either absorbed or scattered by the target. As in the previous section, we then divide the computed cross sections given by eqs.(3) and (5) in three parts, corresponding to absorption of both neutrons, elastic scattering of both neutrons, and absorption of one of them and scattering of the other one. The weight of each of these three contributions is obtained in the optical model for two body systems, and the part of two absorbed neutrons has a weight given by the square of $\sigma_{abs}^{(n)}/(\sigma_{abs}^{(n)} + \sigma_{ela}^{(n)})$, the part of two scattered neutrons has weight given by the square of $\sigma_{ela}^{(n)}/(\sigma_{abs}^{(n)} + \sigma_{ela}^{(n)})$, and finally the part of one neutron absorbed and one scattered has a weight of $2\sigma_{abs}^{(n)}\sigma_{ela}^{(n)}/(\sigma_{abs}^{(n)}+\sigma_{ela}^{(n)})^2$. Again $\sigma_{abs}^{(n)}$ and $\sigma_{ela}^{(n)}$ are the absorption and elastic cross sections obtained by use of an optical potential describing the neutron–target interaction.

This procedure permits then computations of the cross sections for the processes in Fig. 3c where any of the three constituents can be either absorbed or scattered by the target.

In this section we shall apply the method to fragmentation reactions of the two–neutron halo nuclei ^{6}He and ^{11}Li on three different targets, one heavy (Pb) with dominating Coulomb contribution one light (C) with dominating nuclear contribution and an intermediate mass (Cu) with comparable Coulomb and nuclear contributions. We shall first briefly give the specifications leading to the initial wave function. Second we describe how to choose the interactions between target and halo constituents. The last two subsections contain the absolute values of the computed cross sections and the momentum distributions, respectively.

4.1 Three–body wave functions and intrinsic halo interactions

The three–body halo wave functions are obtained by solving the Faddeev equations in coordinate space. This is done by use of the adiabatic hyperspherical approach. The Faddeev equations are written in hyperspherical coordinates, and separated into angular and radial parts. The eigenvalues obtained from the angular part enter into the radial equation as an effective potential. This procedure has previously been successfully used, see for instance [6,34,43].

The neutron–neutron interaction is given in [43]. In the neutron–core interaction for 6He we include s, p and d waves. The parameters are adjusted to reproduce the corresponding phase shifts from zero to 20 MeV. The values are given in [27].

For ^{11}Li we include s and p–waves, and assume spin zero for the core. The parameters for the neutron–core interaction are adjusted to reproduce the available experimental data on ^{10}Li, in particular the presence of a low–lying p–resonance at 500 ± 60 keV with a width of 400 ± 60 keV [46–48], and an even lower lying uncertain virtual s–state at 0.15 ± 0.15 MeV [47,48]. These observed states cannot be used directly in computations assuming zero spin of the ^{9}Li-core. The reason is that the spin splitting, inevitably arising from the finite core spin of 3/2, produces two levels both of s and p-wave character. The measurements refer to the actual (spin-split) levels. Therefore in the present simplified model of zero core spin we must aim at statistically averaged s and p-wave energies, which then necessarily must be above the measured values. We have chosen the realistic model with spin splitting reproducing the available data and simply reduced the spin splitting parameter to zero. The more realistic model with finite core spin is necessary for observables as the two-body invariant mass spectrum, but in most cases the differences are negligibly small [49]. The resulting values for the parameters correspond to potential IV in [20].

It is well known that the use of realistic two–body potentials to describe a three–body system is leading to three–body binding energies too small compared to the experimental values. This is a general problem for few-nucleon systems [50]. For ^{6}He and ^{11}Li the underbinding is around 0.5 MeV and 150 keV, respectively. These deviations are substantial compared to the three-body binding energies, but very small compared to the strengths of the two-body potentials. To recover the experimental value of the binding energy we introduce a phenomenological three-body interaction. The idea is that this three-body force should account for those polarizations of the particles, which are beyond that described by the two-body interactions. Thus, this three-body interaction must be of short range in the hyperradius ρ, since it only contributes when all three particles interact simultaneously. We choose again the gaussian radial shape $V_{3b}(r) = V_3 \exp\left(-\rho^2/b_3^2\right)$, and the parameters for ^{6}He and ^{11}Li are given in [27] and [20], respectively.

Inclusion of these effective three–body interactions together with the neutron–neutron and neutron–core interactions described above give a binding energy and a root mean square radius of 1.0 MeV and 2.50 fm for ^{6}He, and 0.3 MeV and 3.35 fm for ^{11}Li. These numbers are for both nuclei consistent with the experimental values, that are 973.4 ± 1.0 keV [51] and 2.57 ± 0.10 fm [52] for ^{6}He and 295 ± 35 keV [53] and 3.1 ± 0.3 fm [54] for ^{11}Li. One has to realize that what is commonly called *experimental* radius for a halo nucleus is deduced from reaction cross section measurements, and the connection between the few–body wave function and the cross section is model dependent [23]. The real test is therefore the direct comparison between computed and experimental reaction cross sections. The computed ^{6}He wave function corresponds to a probability of roughly 90% relative neutron–core p–waves and about 10% s–waves, while the corresponding numbers for ^{11}Li roughly are 60% relative neutron–core s–waves and 40% p–waves.

4.2 Neutron–target and core–target optical potentials

For the neutron–target interaction we use non–relativistic optical potentials obtained from relativistic potentials through a reduction of the Dirac equation into a Schrödinger–like equation [55]. These phenomenological potentials in the Schrödinger equation produce the same scattering data as obtained by use of the relativistic potentials in the Dirac equation [56]. In particular, we use the energy–dependent, A–independent parameterizations EDAI-C12 and EDAI-Pb208 in [57] for carbon and lead targets, respectively. For copper target we use the energy and A–dependent potential EDAD–fit1 also given in

Table 2
Parameters for the core–target interaction. See eqs.(34) – (38).

Reaction	^{4}He+C	^{4}He+Cu	^{4}He+Pb	^{9}Li+C	^{9}Li+Cu	^{9}Li+Pb
r_v (fm)	1.245	1.245	1.245	1.336	1.336	1.336
r_w (fm)	1.570	1.570	1.570	1.870	1.870	1.870
a_v (fm)	0.751	0.745	0.733	0.900	0.900	0.900
a_w (fm)	0.651	0.635	0.607	0.750	0.750	0.750
a_0 (MeV)	70	110	108	120	220	300
a_1 (MeV)	6.0	6.0	6.0	6.0	6.0	6.0
a_2	–0.008	–0.010	–0.014	–0.008	–0.010	–0.014
b_0 (MeV)	17	21	27	28	28	29
b_1 (MeV)	–1.706	–1.706	–1.706	–1.375	–1.375	–1.375
b_2	0.007	0.007	0.006	0.0025	0.0025	0.006

[57]. In the three cases the potentials fit the scattering data in the nucleon energy range from 20 to 1040 MeV.

For the core–nucleus optical potential we use the parameterization given in [58]. The general shape of this potential is:

$$U(r) = -Vf(r) - iWg(r) + V_{\rm Coul} \tag{34}$$

with form factors of Woods–Saxon type

$$f(r) = (1 + \exp\left[(r - r_v A^{1/3})/a_v\right])^{-1} , \tag{35}$$

$$g(r) = (1 + \exp\left[(r - r_w A^{1/3})/a_w\right])^{-1} , \tag{36}$$

and where $V_{\rm Coul}$ is the Coulomb interaction, and A the mass number of the target. The energy dependence of the potential is contained in the parameters V and W as

$$V(A,Z,E) = a_0 + a_1 Z A^{-1/3} + a_2 E , \tag{37}$$

$$W(A,Z,E) = b_0 + b_1 Z A^{1/3} + b_2 E , \tag{38}$$

where Z is the charge of the target and E is the energy of the projectile.

The parameters used for the different projectiles and targets are given in Table 2. For a ^{6}He projectile the radii, r_v and r_w, and the diffuseness parameters, a_v and a_w, are directly taken from [58]. The strength parameters in eqs.(37) and (38) are also from [58] except for a_2 which is reduced to allow for a large energy variation while simultaneously reproducing the experimental data in [22]. For a ^{11}Li projectile the parameters r_v, r_w, a_v and a_w are from [59], while the parameters in eqs.(37) and (38) are similar to those of ^{6}He but slightly modified to reproduce the available experimental data for ^{9}Li–nucleus scattering [10].

Together with the optical potential we need to specify the value of the distance $R_{cut}^{(j)}$ which is the limiting impact parameter determining whether halo constituent j is participant or spectator. These cutoff parameters play an essential role in the cross sections. If the interaction between constituent i and the target is described by the optical model, the impact parameters for j and k in eqs. (3) and (5) must be limited in accordance with the different geometries in Fig. 3. This is done in practice by including in the overlap eq.(4) only the part of the initial three–body wave function $\Psi^{(JM)}$ such that the distances between particles j–i and k–i are either larger or smaller than the cutoff distances $R_{cut}^{(j)}$ and $R_{cut}^{(k)}$ depending on the reaction in question. We are therefore forcing particles j and k to be inside or outside a sphere around particle i, instead of a cylinder along the beam direction. To do the latter is technically much more difficult, and the use of spheres is a good approximation providing big advantages from the computational point of view.

Several procedures can be followed to obtain these cutoff parameters:

(a) Directly determined from the sizes of the constituent and the target:

$$R_{cut}^{(c)} = r_0\sqrt{A_t^{2/3} + A_c^{2/3}}, \qquad R_{cut}^{(n)} = \sqrt{r_0^2 A_t^{2/3} + R_n^2}\ , \tag{39}$$

where the indices c and n refer to the core and the halo neutron, A_t and A_c are the mass numbers of target and core, and R_n is the neutron radius. The value of the parameter r_0 may vary between 1.1 fm and 1.3 fm.

(b) In the black disk model the absorption cross section for a particle j hitting a target is given by $\pi R_{cut}^{(j)2}$. We can then determine the cutoff radius from measured absorption cross sections. For the projectiles and targets considered in this work some of these experimental data can be found in [10,22,60].

(c) The cutoff radii can also be determined from the measured mean square radii of target ($\langle r^2\rangle_t$) and constituent ($\langle r^2\rangle_j$), which can be found for instance in [61]. The relation to the cutoff radius is then given by

$$\frac{3}{5}R_{cut}^{(j)2} = \langle r^2\rangle_t + \langle r^2\rangle_j + 2\ \ \mathrm{fm}^2\ , \tag{40}$$

where 2 fm^2 is the square of the range of the nucleon interaction. This procedure gives values for $R_{cut}^{(j)}$ very similar to the impact parameter b_g used in eq.(30) to separate high and low impact parameters.

Table 3
The cutoff parameters $R_{cut}^{(j)}$ determined according to the procedures (a), (b) and (c), and the values used in the actual computations.

Target	Method	$R_{cut}^{(n)}$ (fm)	$R_{cut}^{(^4\mathrm{He})}$ (fm)	$R_{cut}^{(^9\mathrm{Li})}$ (fm)
C	(a)	2.7–3.1	3.4–4.7	3.7–5.2
	(b)	2.6–3.0	~ 4.0	~ 4.7
	(c)	3.9	4.2	4.8
	used	3.5	4.0	4.8
Cu	(a)	4.5–5.3	5.2–7.2	5.4–7.6
	(b)	4.9–5.6	~ 6.5	~ 8.5
	(c)	5.5	5.7	6.1
	used	5.4	5.7	6.1
Pb	(a)	6.6–7.8	7.4–10.4	7.6–10.6
	(b)	7.4–7.8	~ 9.0	~ 10.5
	(c)	7.4	7.6	7.9
	used	7.4	7.6	7.9

These three procedures determine the range of variation for $R_{cut}^{(j)}$. The choice of one value or another is a matter of taste, and within the allowed variations these parameters may be used for fine tuning the cross sections. The different values obtained are shown in Table 3 together with the ones actually used in the calculations. We see that the range of variation of the cutoff is rather small for the neutron, and its value consequently is rather precisely determined. The same happens for ^{4}He and ^{9}Li on a carbon target, while for heavier targets like Cu, and especially for Pb, the cutoff radii vary more.

The adiabatic cutoff energy in eq.(29) is chosen as $\hbar\omega_a = 1$ MeV for ^{6}He and 0.15 MeV for ^{11}Li, corresponding to the three-body binding energy and half of it, respectively. This means that ^{11}Li in the sharp cutoff model breaks up corresponding to virtual photon energies down to half of the binding energy. The agreement with measured values discussed in the next section then indicates a connection with the soft structure revealed in the low lying dipole strength [17,24,27,28]. The high energy tail of the virtual photon spectrum must efficiently produce breakup of ^{11}Li [44].

In Fig. 4 we show two–neutron removal cross sections obtained after fragmentation of ^{6}He and ^{11}Li on C (left part), Cu (central part) and Pb (right part). In the three cases the long–dashed line shows the contribution to the cross section from elastic scattering of the core by the target (core participant), while the short–dashed line is the contribution from processes where the core is spectator.

For a carbon target the core participant contribution is only significant at low beam energies, where it contributes by up to 25% of the total cross section for the ^{6}He projectile, and somewhat less for ^{11}Li. For large beam energies this contribution is at most 10% of the total. The main contribution is given by processes where the core is a spectator, and only the halo neutrons interact with the target. This contribution is shown by the short–dashed line in the figure as computed from the second and third terms in eq.(32). These two terms contain contributions from the reactions in Fig. 3a, where one of the neutrons and the core are spectators, and from the reaction in Fig. 3b, where only the core is a spectator. For comparison we also show in the figure the two–neutron removal cross section obtained only from the reactions in Fig. 3a where one neutron and the core are spectators (dot–dashed curve).

In the central part we show the results for a Cu target. Due to the Coulomb interaction the core participant contribution dominates at low beam energies, but decreases below that of the core spectator with increasing energy. For the ^{6}He projectile this crossing appears at a beam energy of around 600 MeV/nucleon clearly larger than the 100 MeV/nucleon for ^{11}Li. Therefore, for energies from 100 MeV/nucleon to 600 MeV/nucleon the main contribution to σ_{-2n} comes from core participant reactions for ^{6}He projectile and from core spectator reactions for ^{11}Li projectile. In other words, a Cu target resembles a light target for the ^{11}Li projectile and a heavy target for ^{6}He. This is due to the larger size of ^{11}Li compared to the one of ^{6}He.

The general behavior of σ_{-2n} for heavy targets is seen in the right hand side of Fig. 4, where the results for a Pb target are shown. Due to the large Coulomb interaction the core participant contribution is clearly dominating, see the dot–dashed line corresponding to the reaction in Fig. 3d, where only the large impact parameter part ($q < q_g$) of the Coulomb interaction is included. This contribution is for both projectiles very similar to the one coming from core participant (dashed), that includes the full Coulomb core–target interaction, the nuclear core–target interaction, and the interference between them. The contribution given by the neutron–target interaction (core spectator, dotted) is negligible at low beam energies for both projectiles, while at large beam energies it contributes around 15% of the total for ^{6}He and 35%

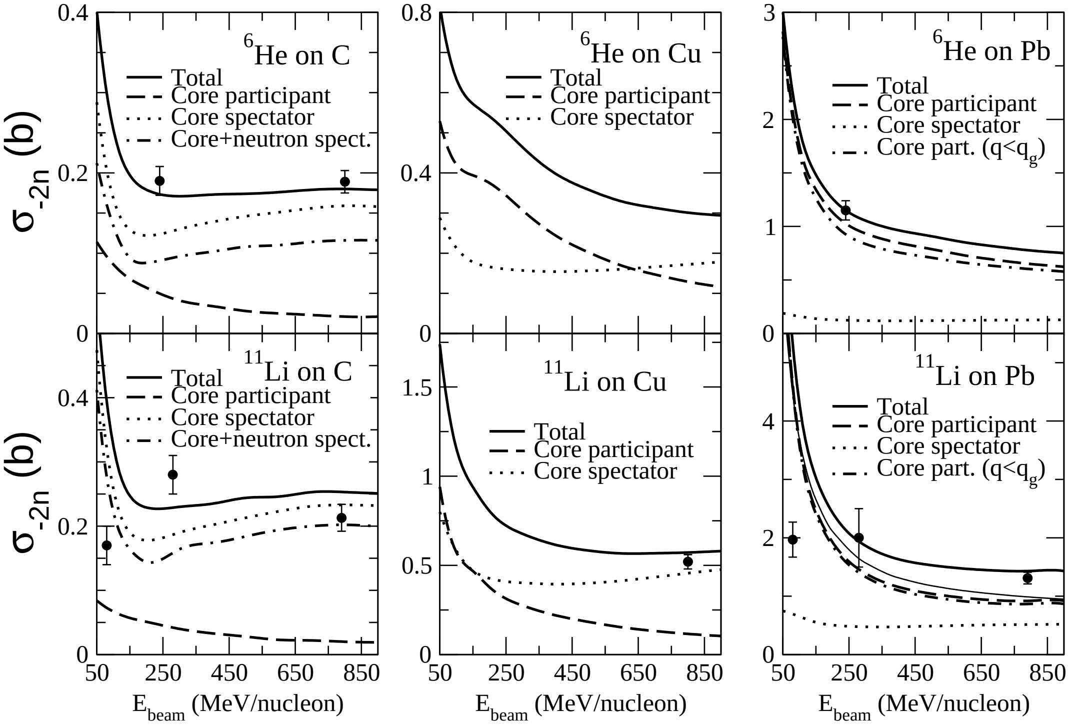

Fig. 4. Total two–neutron removal cross section, eq.(31), after fragmentation of ^{6}He and ^{11}Li on carbon (left), copper (middle) and lead (right) as function of beam energy. The long–dashed and short–dashed lines are the contributions to the total from participant core and core spectator, respectively. In the carbon case the dot–dashed line is the contribution assuming that the core and one of the halo neutrons are spectators. In the lead case the dot–dashed line is the large impact parameter contribution of the Coulomb interaction (Fig. 3d). For ^{11}Li on Pb the thin solid line is the total two–neutron removal cross section for $\hbar\omega_a$= 0.3 MeV (see text). The experimental data are from [7,8,10,14,17].

of the total for ^{11}Li. The agreement with the measured values is overall rather good considering the incompatibility of some of the data points. As mentioned at the end of the previous section, the adiabatic cutoff $\hbar\omega_a$ is chosen to be 0.15 MeV for the ^{11}Li projectile. The result of the expected logarithmic dependence on $\hbar\omega_a$ is shown in Fig. 4 for the two-neutron removal cross section for the Pb target where the effect is largest. The thin line shows the computed cross section with $\hbar\omega_a$= 0.3 MeV. The agreement with the experimental points is only slightly worse. For the C target the minimum value of the momentum transfer is given by q_L instead of q_a (see sect. 2.3), and for Cu target q_L becomes larger than q_a for beam energies around 150 MeV/nucleon when $\hbar\omega_a = 0.15$ MeV and around 400 MeV when $\hbar\omega_a = 0.3$ MeV. Therefore the choice of one value or the other for the adiabatic cutoff energy does not play any role for C target and insignificant for the Cu target. For ^{6}He projectile we used $\hbar\omega_a = 1$ MeV, corresponding to its binding energy. A variation of this number within a reasonable range produces a smaller change than in the case of ^{11}Li due to its smaller charge.

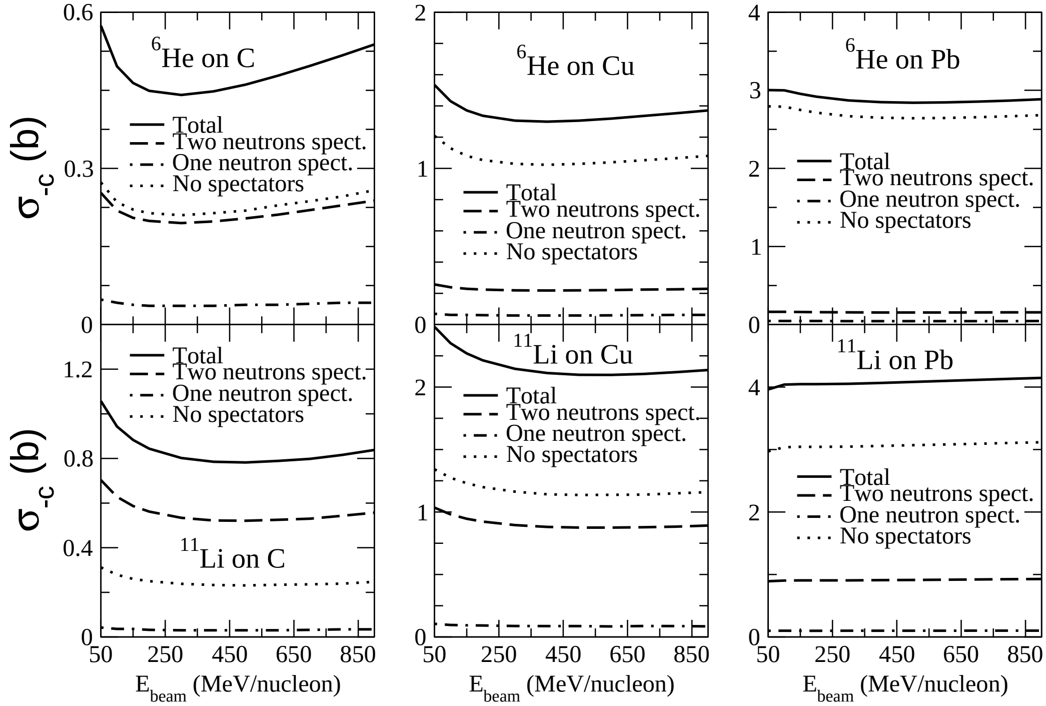

Fig. 5. Total core breakup cross sections, eq.(31), after fragmentation of ^{6}He and ^{11}Li on carbon (left), copper (middle) and lead (right) as function of beam energy. The long–dashed, dot–dashed and short–dashed lines are the contributions to the total from the reactions in Fig. 3a (two neutrons spectators), Fig. 3b (one neutron spectator) and Fig. 3c (no spectators).

In Fig. 5 we show core breakup cross sections after fragmentation of ^{6}He and ^{11}Li on C (left), Cu (middle) and Pb (right). For the three targets we have plotted the contributions from the reactions in Fig. 3a, where the core is absorbed while the two neutrons are spectators (long–dashed line), the contributions from the reactions in Fig. 3b where only one of the halo neutrons is spectator (dot–dashed curve), and the contribution from the reaction in Fig. 3c, where there are no spectators (short–dashed line).

For a carbon target we see that for the ^{11}Li projectile the contribution from the two–neutron spectators is dominant, and the contribution from simultaneous collisions with the target of more than one constituents is smaller, although still significant. For the ^{6}He projectile the situation is different, and the no spectators contribution is even larger than the two–neutron spectators contribution. This is a reflection of the difference in size between these projectiles. If we denote the neutron–core distance r_{nc} we obtain $\langle r_{nc}^2\rangle^{1/2} = 4.2$ fm for ^{6}He and $\langle r_{nc}^2\rangle^{1/2} = 5.9$ fm for ^{11}Li. In ^{6}He the two halo neutrons are then closer to the core than in ^{11}Li. Thus, when the core is absorbed the two halo neutrons have a larger probability of being spectators for ^{11}Li than for the ^{6}He projectile.

For a copper target the no spectators contribution is dominant for core

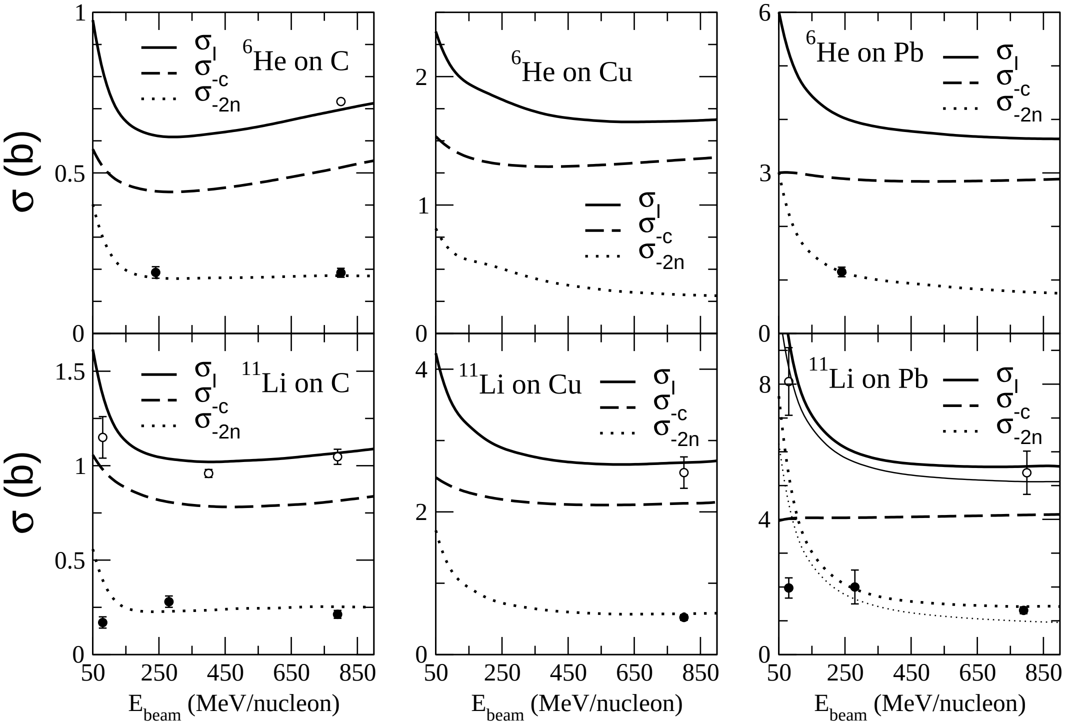

Fig. 6. Total interaction (solid), two–neutron removal (long–dashed) and core breakup (short–dashed) cross sections after fragmentation of ^{6}He and ^{11}Li on carbon (left), copper (middle) and lead (right). For ^{11}Li on Pb the thin solid and dotted lines are the interaction and two–neutron removal cross section for $\hbar\omega_a$= 0.3 MeV (see text). Experimental data are from [7,8,10,14,17,22].

destruction for both projectiles. Changing from C to Cu we increase the size of the targets, and therefore the probability for the halo neutrons being spectators decreases. Again the smaller size of ^{6}He is responsible for the larger difference between the long–dashed and short–dashed curves compared to the case of ^{11}Li projectile. The same behavior is observed for a Pb target. As the target mass increases the probability for the two neutrons being spectators decreases. The dominant process for a heavy target is the one where all the three halo constituents interact with the target.

In Fig. 6 we plot interaction cross sections for the two projectiles and the three targets that we are considering. They are cross sections corresponding to processes where the projectile undergoes some reaction, and they are given by the sum of the two–neutron removal and core breakup cross sections. As a general rule σ_{-c} is larger than σ_{-2n}, and only for low beam energies and heavy targets σ_{-2n} dominates due to the large distance Coulomb collisions maintaining the core intact. Again, for ^{11}Li on Pb the computed interaction and two-neutron removal cross sections differ somewhat when the adiabatic cutoff energy $\hbar\omega_a$ is increased from 0.15 MeV to 0.30 MeV.

The agreement with the experimental data is good, except for the low beam energy point for the ^{11}Li projectile. However, this experimental point

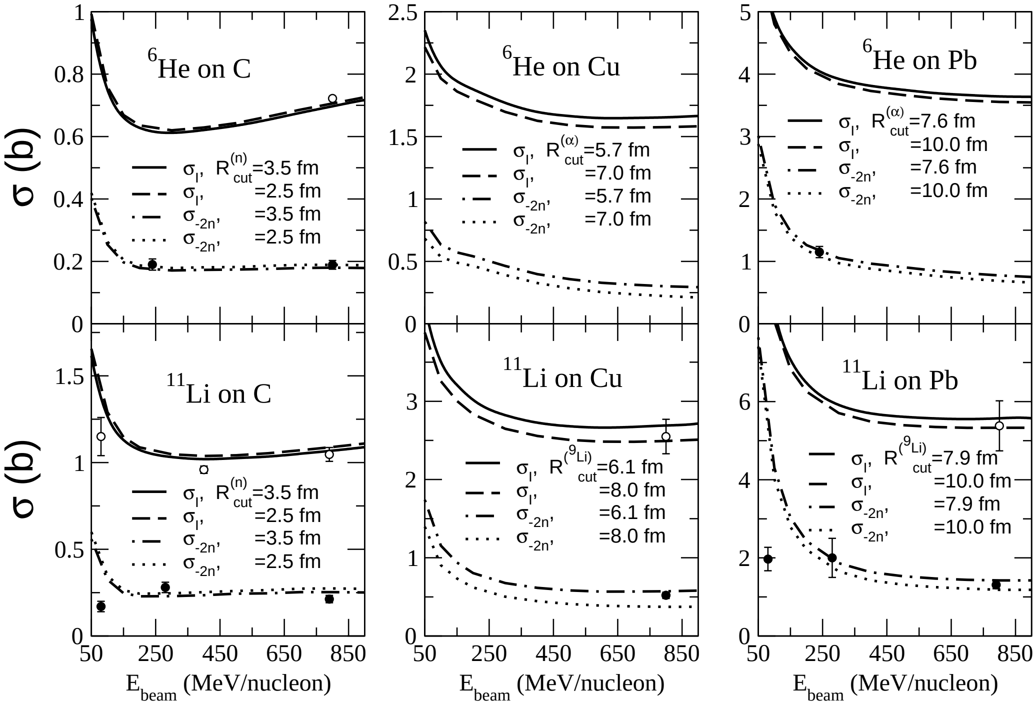

Fig. 7. Interaction and two–neutron removal cross sections for ^{6}He and ^{11}Li on C, Cu and Pb for different values of the cutoff parameters.

should be taken with caution, since the σ_{-2n} values for C and Pb targets are not consistent with the data for ^{11}Li on beryllium or gold, for which the experimental values of σ_{-2n} at 30 MeV/nucleon are 0.47 ± 0.10 b and 5.0 ± 0.8 b, respectively [62].

As shown in Table 3 the values of the cutoff parameters $R_{cut}^{(j)}$ are not uniquely determined. In Fig. 7 we examine the dependence of the interaction and two–neutron removal cross sections on these parameters. For a carbon target the main uncertainty appears in the case of a neutron spectator, where the value of $R_{cut}^{(n)}$ can vary between 2.6 fm and 3.9 fm. We used 3.5 fm in the previous calculations. In Fig. 7 we compare the cross sections with $R_{cut}^{(n)}$=2.5 fm and 3.5 fm, while we maintain 4.0 fm and 4.8 fm for $R_{cut}^{(^4\mathrm{He})}$ and $R_{cut}^{(^9\mathrm{Li})}$, respectively. The difference between these two calculations is very small. For Cu and Pb targets the largest range of variation for the cutoff parameters is for the core spectator. In the calculations shown up to now we have chosen the value obtained with procedure c), but procedures a) and b) can give significantly larger values for these parameters, see Table 3.

In Fig. 7 we also compare σ_I and σ_{-2n} obtained with $R_{cut}^{(^4\mathrm{He})} = 5.7$ fm and 7.0 fm and $R_{cut}^{(^9\mathrm{Li})} = 6.1$ fm and 8.0 fm for a Cu target, and $R_{cut}^{(^4\mathrm{He})} = 7.6$ fm and 10.0 fm and $R_{cut}^{(^9\mathrm{Li})} = 7.9$ fm and 10.0 fm for a Pb target. It is then striking that even when the difference between the parameters is substantial, the difference between the computed cross sections is rather insignificant. The main reason

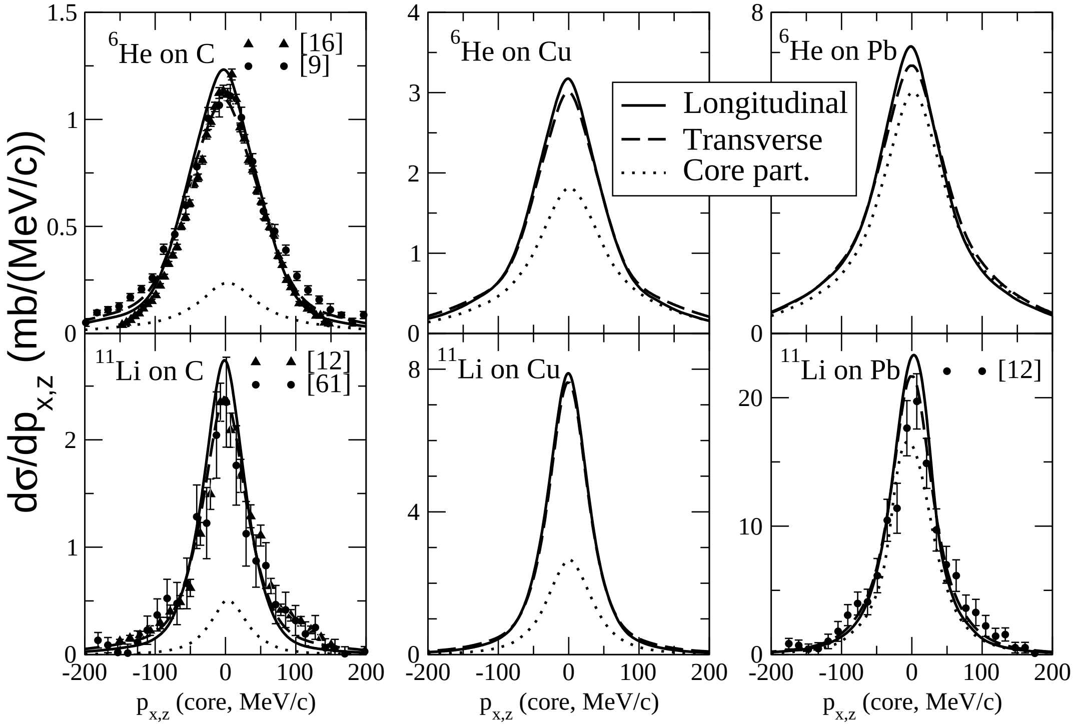

Fig. 8. Longitudinal (solid) and transverse (long–dashed) core momentum distributions after fragmentation of ^{6}He and ^{11}Li on C, Cu and Pb. The short–dashed line shows the contribution from core participant. Experimental data are from [9,16] for ^{6}He on C, from [12,63] for ^{11}Li on C and from [12] for ^{11}Li on Pb. The experimental data have been scaled to the calculations.

is that for these two targets an important contribution comes from the large impact parameter part of the Coulomb contribution (the reaction in Fig. 3d), where the cutoff parameters are unimportant. This is especially true for the lead target with the large Coulomb interaction.

The main conclusion obtained from Fig. 7 is that the value chosen for the cutoff parameters within the range shown in Table 3 is not substantially modifying the cross sections. We may view these parameters as relevant for fine tune, while the cross section sizes and general behavior are maintained.

4.4 Momentum distributions

In Fig. 8 we show the longitudinal and transverse core momentum distributions after fragmentation of ^{6}He and ^{11}Li on on C, Cu and Pb. The calculations have been done at a beam energy of 300 MeV/nucleon. For this energy the difference between longitudinal and transverse momentum distributions is small. The transverse distributions are in general wider than the longitudinal, typically by 6 to 12 MeV/c. The experimental data are taken from [9,16] for ^{6}He on C, and they are obtained at a beam energy of 400 MeV/nucleon and 240 MeV/nucleon, respectively. For ^{11}Li on C the experimental data are taken from [12,63] and they have been obtained with a beam energy of 280 MeV/nucleon. For ^{11}Li on Pb the data are from [12] and they correspond to a beam energy of 280 MeV/nucleon. Within this range of energies the difference in shape between the computed distributions is not visible. In all the cases the experimental data are given in arbitrary units, and they have been scaled to the calculations. The agreement between them and the calculations is good.

In Fig. 8 the short–dashed line shows the contribution from core participant. For light targets the dominating processes are those where the core is not participant, and therefore its final momentum is similar to the one that it had inside the halo projectile (except for the final neutron–core interaction, that does not modify significantly the core momentum [35]). When the target size increases the weight of the core participant contribution becomes more important. For Pb this contribution is very close to the total. The dominating process is then the one shown in Fig. 3d, where only the low momentum transfer part of the Coulomb interaction should be included. The momentum transferred to the core in the collision is small compared to its initial momentum distribution, which therefore for a entirely different reason again is left relatively unchanged. Although in this case the three–body continuum wave function should be used, only the final neutron–neutron interaction has been included. Nevertheless, due to its large mass, core momentum distributions are not expected to be strongly modified by the final state interaction [34,35]. The consequence is that the shape of the core momentum distributions is almost independent of the target. Only the initial core momentum distribution within the projectile is decisive.

In Fig. 9 we show longitudinal and transverse neutron momentum distributions after two–neutron removal fragmentation of ^{6}He and ^{11}Li on C, Cu and Pb. The calculations have been performed at a beam energy of 300 MeV/nucleon. The difference between longitudinal and transverse distributions is very small. Usually the computed transverse distributions are from 2 to 4 MeV/c wider, and the difference between them is hardly visible.

As in Fig. 8 the short–dashed curve shows the contribution from core–participant processes. The behavior is similar to the one found in Fig. 8. For light targets the core spectator contribution is dominating, while for heavy targets the main contribution comes from processes where the core participates. The only available experimental neutron momentum distribution is for ^{6}He on C [16] obtained at a beam energy of 240 MeV/nucleon. The agreement with the experiment is excellent, and only in the tails the computed curve is above the experimental distribution. This is due to the experimental neutron acceptance, that is limited in horizontal and vertical directions to a momentum of 50 MeV/c.

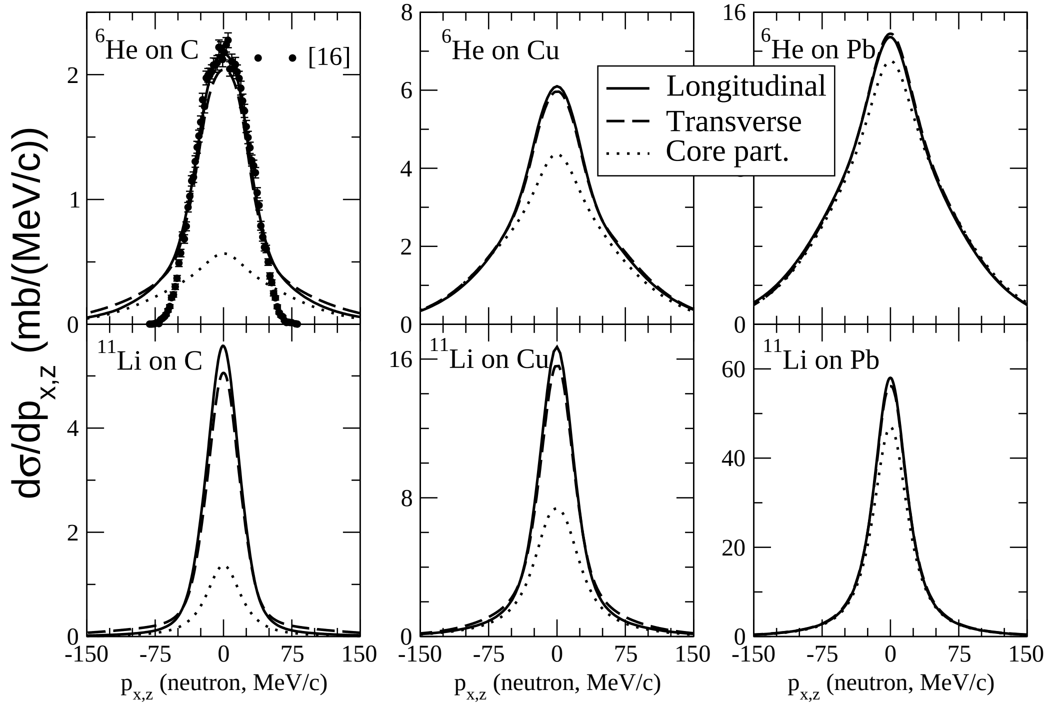

Fig. 9. The same as in Fig. 8 for neutron momentum distributions. The experimental data for ^{6}He on C are from [16].

For a lead target the neutron momentum distribution is dominated by core participant processes, and in particular by processes where the momentum transferred to the core is small. As discussed in Section 2, the final state is properly described for relatively small impact parameters by the reaction scheme shown in Fig. 1. For heavy targets the reaction is dominated by processes where mainly the low momentum transfer part of the Coulomb interaction contributes. The breakup process is then relatively gentle, and the three–body continuum wave function should be used to describe the final state as shown in Fig. 2. Therefore Eqs.(8) and (18) should then be used to describe these processes.

It is well known that neutron momentum distributions are highly influenced by the final state interaction between fragments, while this influence is less important for core momentum distributions [34,35] due to the larger mass. In Figs. 8 and 9 we computed all distributions using the reaction scheme of Fig. 1, and therefore for the case of Pb target, where the final three–body continuum wave function should be used, only the final neutron-neutron interaction is included. As mentioned this has only a small influence on the core momentum distributions, where the agreement with the experiment shown in Fig. 8 is satisfactory. However, the computed neutron momentum distributions after fragmentation on a heavy target like Pb shown in Fig. 9 are expected to be too broad compared to the experimental data due to the neglect of the final state interaction between the neutron and the core for the dominating process.

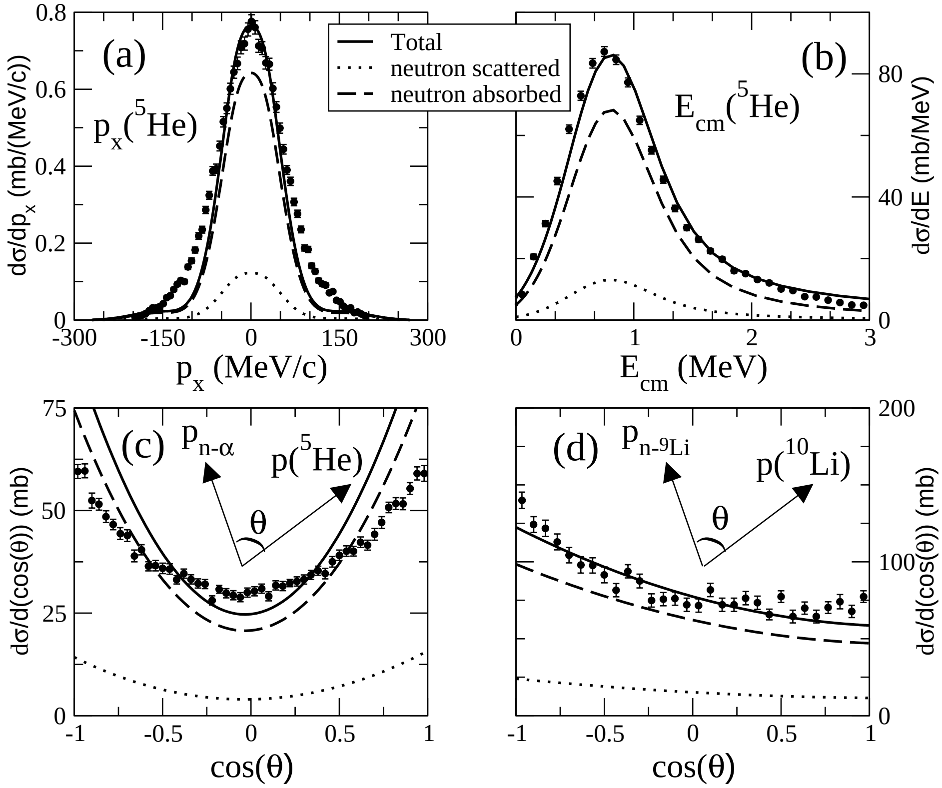

Fig. 10. Various distributions obtained after fragmentation of ^{6}He and ^{11}Li on C at 300 MeV/nucleon. We only include the dominating parts where the α particle and one neutron are spectators. (a) is the transverse distribution of the ^{5}He center of mass momentum, (b) is the invariant mass spectrum of ^{5}He, (c) is the angular distribution with θ as the angle between the relative α–neutron momentum and the center of mass momentum of ^{5}He, and (d) is the the same as (c) for a ^{11}Li projectile. The computed distributions have been convoluted with the instrumental response [65]. The experimental data are from [16] in (a) and (b), from [15] in (c) and from [66] in (d).

These computed results, including the neutron-neutron final state interaction, are still much more realistic than the Fourier transform of the initial wave function implying that all final state interactions are neglected.

For completeness we show in Fig. 10 four other interesting observables obtained after fragmentation of ^{6}He and ^{11}Li. As discussed above, inclusion of all the final state interactions is required for heavy targets corresponding to reaction scheme Fig. 2. Thus we focus here only on a C target. Similar observables for the ^{11}Li projectile are already published in [20]. The calculations are performed for a beam energy of 300 MeV/nucleon, and the experimental data in Figs. 10a and 10b from [16] and in Fig. 10c from [15] are given in arbitrary units for a beam energy of 240 MeV/nucleon. The ones in Fig. 10d from [66] are also given in arbitrary units for a beam energy of 287 MeV/nucleon. In ref.[64], where angular distributions for ^{6}He projectile are shown, we inadvertently used a wrong relative phase between interfering two-body final states. The conclusions in [64] still hold but the numerical results now compare slightly better with measured values.

The calculations in Fig. 10 are in agreement with the experiments, except for the angular distribution in Fig. 10c. The main reason for this discrepancy is due to the approximation of spheres instead of the proper cylinder geometries shown in Figs. 1 and 2. The exceptional sensitivity arises in this case, because the dependence on $\cos\theta$ of the components with neutron-core relative p-wave angular momentum projection $m = \pm 1$ are very flat while the $m = 0$ component is strongly varying [64]. Unlike the other quantities the proper cutoff symmetry is then decisive for this particular observable. The cylinder would remove relatively more of the $m = 0$ component of the neutron-core p-wave and the computation would approach the measured distribution. The angular distributions are very different for ^{6}He and ^{11}Li projectiles as seen by comparing Figs. 10c and 10d. The large average value for ^{10}Li reflects the dominating constant contribution from neutron-core relative s-waves and the asymmetric variation is due to the interference of s and p-waves. The strong dependence on the proper cutoff of the different angular momentum projection states is then not present. It is especially interesting that the angular distribution for ^{10}Li in Fig. 10d agrees so well since these computations were performed before the measurements were available.

5 Summary and conclusions

In this paper we formulate a model to describe fragmentation reactions of two–neutron halo nuclei on any nuclear target, from light to heavy. It is well established that nuclear and Coulomb interactions dominate for light and heavy targets, respectively. Thus both must be incorporated in a comprehensive description which also should include intermediate target masses. We confine ourselves to relatively high energies where the reaction time can be expected to be short compared to the time scale of the intrinsic halo motion.

The structure computations proceed in two steps, i.e. few-body models are used to describe the halo degrees of freedom and then the effects of the intrinsic structure of the halo constituents are considered. We adopt the same two-step strategy and start with a reaction model for weakly bound inert halo particles. Due to the spatial extension of the initial three-body system the dominating processes for short-range interactions are independent reactions of each halo particle (participant) with the target as for free particles. The participant is then elastically scattered or “something else” called absorption happens while the other two halo particles (spectators) continue undisturbed under the influence of their mutual interaction.

We use the optical model to describe the participant-target interaction. Elastic scattering is then described in details while different processes are considered as absorption which means that all other channels only remove probability and otherwise forgotten. However, this is the essence of the information in breakup experiments where the forward fragmentation products are measured. Furthermore, absorption in this optical model sense accounts for intrinsic degrees of freedom related to the target and the halo constituents. This is in other words consistent with the use of a three-body model for the halo structure. Going beyond this approximation in the reaction description requires at least as accurate a treatment of core degrees of freedom of the initial state.

Another crucial ingredient to understand the reaction mechanisms is the finite sizes of both halo constituents and target. Conceptually this is related to the necessity both of accounting for intrinsic degrees of freedom and for describing more than one simultaneous halo particle interaction with the target. This becomes clear in the impact parameter picture where more than one particle at the same time may arrive at the target position within the interaction cylinder. We characterize the different processes of absorption and/or elastic scattering of the different halo particles that simultaneously interact with the target. For one of them (the core if possible) we employ optical potentials, and for the other(s) we use the part of the three–body wave function where this constituent is close enough to the first one such that it can be considered to be inside its cylinder. The model provides absolute cross sections for all different processes.

So far we discussed the short-range parts of the interactions. In the impact parameter picture we may more conveniently formulate this as a restriction to relatively large momentum transfer to the participant. Then the reaction mechanism is basically independent halo particle reactions dictating the division into two independent two-body final state systems (spectators and participant-target) and in our formulation resulting in the participant-spectator model. This division is not for convenience of computation but to include the proper physics.

The large impact parameters or equivalently the small momentum transfers are important for long-range interactions. For nuclear halos this means the Coulomb interaction which is active when the charged core is a participant. When the target is heavy with a high charge this gives rise to the main contribution to the breakup cross sections arising from very distant collisions. The momentum transfer to the core then excites low lying states of the halo which for Borromean systems imply the low lying continuum states. These collisions are gentle and none of the halo particles are absorbed. Consequently the final state must consist of the three-body halo system and an independent target. The model distinguishes for these reasons between small and large momentum transfer and allows therefore simultaneous treatment of nuclear and Coulomb interactions including interference terms.

We use the model to investigate fragmentation reactions of ^{6}He and ^{11}Li on different targets, light as carbon, intermediate as copper, and heavy as lead. Total interaction, two–neutron removal and core breakup cross sections are computed as function of beam energy and found to be in good agreement with the available experimental data. We compute not only the terms arising from the dominating reaction mechanism, but also the parts usually neglected: Coulomb contribution for light targets and nuclear contribution for heavy targets. Reaction cross sections with targets of intermediate mass and charge, where nuclear and Coulomb interaction interfere and give comparable contributions, are also calculated. The model parameters are obtained from independent sources like nuclear radii, binding energies and two-body scattering experiments.

The cross sections for reaching the different final states consisting of the non-absorbed particles vary with target, projectile and beam energy. For light targets two neutrons and no core is most probable while all three halo particles or the core alone is least probable. For heavy targets absorption of all three particles is most probable except at low beam energies where simultaneous survival of all three halo particles is most probable. The smallest probability is found for core survival alone or the core with one neutron.

Core destruction is more probable than two-neutron removal for all energies and targets. Core destruction receives the largest contribution for heavy targets when all halo particles are absorbed while for light targets the two-neutron spectator contribution is comparable in size. Two-neutron removal receives for heavy targets the largest contributions from core participation while for light targets the largest contribution arises from the core as a spectator. The relative sizes of all these cross sections reflect the reaction mechanisms which in this way are open for experimental tests.

We have also computed core and neutron momentum distributions after fragmentation. This is a strong test of validity of the model, since total values obtained after integration could be in good agreement with experiments even when the non-integrated differential cross sections differ from measurements.

It is known that final state interactions play an essential role in the momentum distributions, especially for light particles as neutrons. For light targets the dominant reactions are the ones with one or two spectators, and the model accounts properly for the final state interaction between spectators. The neutron momentum distribution receives a narrow contribution from one-neutron absorption and a broader contribution from neutron participation and subsequent scattering. The agreement with the available experimental core and neutron momentum distributions is excellent for both projectiles.

For heavy targets the low momentum transfer reaction dominates, and the appropriate reaction mechanism involves the low lying three-body continuum excitations in the final state. This implies that all three initial three-body interactions are necessary in the final state. In the numerical examples we only included two at a time. For core momentum distributions, where the final state interactions are expected to be less relevant, we still obtain good agreement with the experiment. For neutron momentum distributions we include the neutron-neutron interaction but not the neutron-core interaction. The distributions are therefore expected to be somewhat too broad.

The model predicts comparable shapes for core and neutron momentum distributions for light and heavy targets although the reaction mechanisms are very different. For light targets one-neutron absorption is the dominating process leaving the other neutron and the core untouched in the final state under their mutual interaction. For heavy targets the dominating process is a distant collision of low momentum transfer to the core leaving the two neutrons untouched and the core with a momentum very close to its initial value. Still the three particles are influenced by the final state interactions. In both cases the core and the neutrons would appear basically with their initial momentum distributions modified by final state interactions. This is not tested in details, but still in qualitative agreement with experiments.

The model describes a number of different reaction mechanisms and provides the appropriate relative weights for the corresponding processes. The same consistent model with one set of parameters is used throughout for all observables. In this paper the model is tested in details by comprehensive calculations for the most studied two-neutron halo nuclei. This includes absolute values of the differential cross sections as functions of beam energy and target. Dominating contributions to many relative distributions can sometimes be explained by simpler models since they are surface or tail dominated. However, the intrinsic degrees of freedom are necessary to obtain reliable absolute values, especially for less dominating processes. The details are unnecessary for breakup reactions as long as predictable total removal probabilities can be obtained as provided by the phenomenological optical model.

In conclusion, the model seems to be very successful but the many predictions should be tested by experiments to tie down in details the correct reaction mechanisms.

Acknowledgement. We thank K. Riisager and E. Nielsen for continuous discussions and suggestions.

References

[1] K. Riisager, Rev. Mod. Phys. **66** (1994) 1105.

[2] P.G. Hansen, A.S. Jensen and B. Jonson, Ann. Rev. Nucl. Part. Sci. **45** (1995) 591.

[3] I. Tanihata, J. Phys. **G22** (1996) 157.

[4] B. Jonson and K. Riisager, Phil. Trans. R. Soc. Lond. **A356** (1998) 2063.

[5] M.V. Zhukov, B.V. Danilin, D.V. Fedorov, J.M. Bang, I.J. Thompson and J.S. Vaagen, Phys. Rep. **231** (1993) 151.

[6] E. Nielsen, D.V. Fedorov, A.S. Jensen and E. Garrido, Phys. Rep. in press.

[7] I. Tanihata et al., Nucl. Phys. **A488** (1988) 113c.

[8] T. Kobayashi et al., Phys. Lett. **B232** (1989) 51.

[9] T. Kobayashi, Nucl. Phys. **A538** (1992) 343c.

[10] B. Blank *et al.*, Nucl. Phys. **A555** (1993) 408.

[11] T. Nilsson *et al.*, Europhys. Lett. **30** (1995) 19.

[12] F. Humbert *et al.*, Phys. Lett. **B347** (1995) 198.

[13] N.A. Orr et al., Phys. Rev. **C51** (1995) 3116.

[14] M. Zinser et al., Nucl. Phys. **A619** (1997) 151.

[15] L.V. Chulkov et al., Phys. Rev. Lett. **79** (1997) 201.

[16] D. Aleksandrov et al., Nucl. Phys. **A633** (1998) 234.

[17] T. Aumann et al., Phys. Rev. **C59** (1999) 1252.

[18] H. Simon, Ph.D. Thesis, Technische Universität, Darmstadt (1998).

[19] G.F. Bertsch, K. Hencken and H. Esbensen, Phys. Rev. **C57** (1998) 1366.

[20] E. Garrido, D.V. Fedorov and A.S. Jensen, Phys. Rev. **C59** (1999) 1272.

[21] Y. Ogawa, K. Yabana and Y. Suzuki, Nucl. Phys. **A543** (1992) 722.

[22] Y. Suzuki, T. Kido, Y. Ogawa, K. Yabana and D. Baye, Nucl. Phys. **A567** (1994) 957.

[23] J.S. Al-Khalili and J.A. Tostevin, Phys. Rev. Lett. **76** (1996) 3903.

[24] Y. Suzuki and Y. Tosaka, Nucl. Phys. **A517** (1990) 599.

[25] C.A. Bertulani and L.F. Canto, Nucl. Phys. **A549** (1992) 163.

[26] P. Banerjee, J.A. Tostevin and I.J. Thompson, Phys. Rev. **C58** (1998) 1337.

[27] A. Cobis, D.V. Fedorov and A.S. Jensen, Phys. Rev. **C58** (1998) 1403.

[28] C.A. Bertulani, L.F. Canto and M.S. Hussein, Phys. Rep. **226** (1993) 281.

[29] F. Barranco, E. Vigezzi and R.A. Broglia, Phys. Lett. **B319** (1993) 387.

[30] E. Garrido, D.V. Fedorov and A.S. Jensen, Europhys. Lett. **50** (2000) 735.

[31] E. Garrido, D.V. Fedorov and A.S. Jensen, Phys. Lett. **B480** (2000) 32.

[32] S.N. Ershov, B.V. Danilin and J.S. Vaagen, Phys. Rev. **C62** (2000) 041001.

[33] E. Garrido, D.V. Fedorov, A.S. Jensen and K. Riisager, Phys. Rev. Lett., in press.

[34] E. Garrido, D.V. Fedorov and A.S. Jensen, Phys. Rev. **C53** (1996) 3159.

[35] E. Garrido, D.V. Fedorov and A.S. Jensen, Phys. Rev. **C55** (1997) 1327.

[36] P.G. Hansen, Phys. Rev. Lett. **77** (1996) 1016.

[37] E. Garrido, D.V. Fedorov and A.S. Jensen, Europhysics Lett. **43** (1998) 386.

[38] J. Bang and C.A. Pearson, Nucl. Phys. **A100** (1967) 1.

[39] G.R. Satchler, Direct reactions (Oxford Press, New York, 1983) sect. 3.4, 3.5, 3.6.

[40] P.G. Hansen and B. Jonson, Europhys. Lett. **4** (1987) 409.

[41] A.G. Sitenko and P.J. Shepherd, Lectures in Scattering Theory, (Pergamon Press, 1971) pp. 228, 238.

[42] J.A. Tostevin, R.C. Johnson and J.S. Al-Khalili, Nucl. Phys. **A630** (1998) 340c.; R.C. Johnson, J.S. Al-Khalili, and J.A. Tostevin, Phys. Rev. Let. **79** (1997) 2771

[43] E. Garrido, D.V. Fedorov and A.S. Jensen, Nucl. Phys. **A617** (1997) 1.

[44] C.A. Bertulani and G. Baur, Phys. Rep. **163** (1988) 299.

[45] J.D. Jackson, Classical Electrodynamics, (John Wiley & Sons, New York, 1975) pp. 619.

[46] B.M. Young et al., Phys. Rev. **C49** (1994) 279.

[47] S.N. Abramovich, B.Ya. Guzhovskij and L.M. Lazarev, Phys. Part. Nucl. **26** (1995) 423.

[48] J.A. Caggiano, D. Bazin, W. Benenson, B. Davids, B.M. Sherill, M. Steiner, J. Yurkon, A.F., Zeller and B. Blank, Phys. Rev. **C60** (1999) 064322.

[49] D.V. Fedorov, E. Garrido and A.S. Jensen, Phys. Rev. **C51** (1995) 3052.

[50] J. Carlson and R. Schiavilla, Rev. Mod. Phys. **70** (1998) 743.

[51] G. Audi and A.H. Wapstra, Nucl. Phys. **A595** (1995) 409.

[52] L.V. Chulkov, B.V. Danilin, V.D. Efros, A.A. Korsheninnikov and M.V. Zhukov, Europhys. Lett. **8** (1989) 45.

[53] B.M. Young et al., Phys. Rev. Lett. **71** (1993) 4124.

[54] I. Tanihata et al., Phys. Lett. **B287** (1992) 307.

[55] J.M. Udías, P. Sarriguren, E. Moya de Guerra, E. Garrido and J.A. Caballero, Phys. Rev. **C51** (1995) 3246.

[56] H.S. Sherif, R.I. Sawafta and E.D. Cooper, Nucl. Phys. **A449** (1986) 709.

[57] E.D. Cooper, S. Hama, B.C. Clark and R.L. Mercer, Phys. Rev. **C47** (1993) 297.

[58] M. Nolte, H. Machner and J. Bojowald, Phys. Rev. **C36** (1987) 1312.

[59] M. Zahar et al., Phys. Rev. **C54** (1996) 1262.

[60] W. Schimmerling, T.J. Devlin, W.W. Johnson, K.G. Vosburgh and R.E. Mischke, Phys. Rev. **C7** (1973) 248.

[61] H. de Vries, C.W. de Jager and C. de Vries, At. Data Nucl. Data Tables **36** (1987) 495.

[62] K. Riisager et al., Nucl. Phys. **A540** (1992) 365.

[63] H. Geissel and W. Schwab, Private communication.

[64] E. Garrido, D.V. Fedorov and A.S. Jensen, Phys. Rev. **C58** (1998) R2654.

[65] H. Emling, Private communication.

[66] H. Simon et al., Phys. Rev. Lett. **83** (1999) 496.

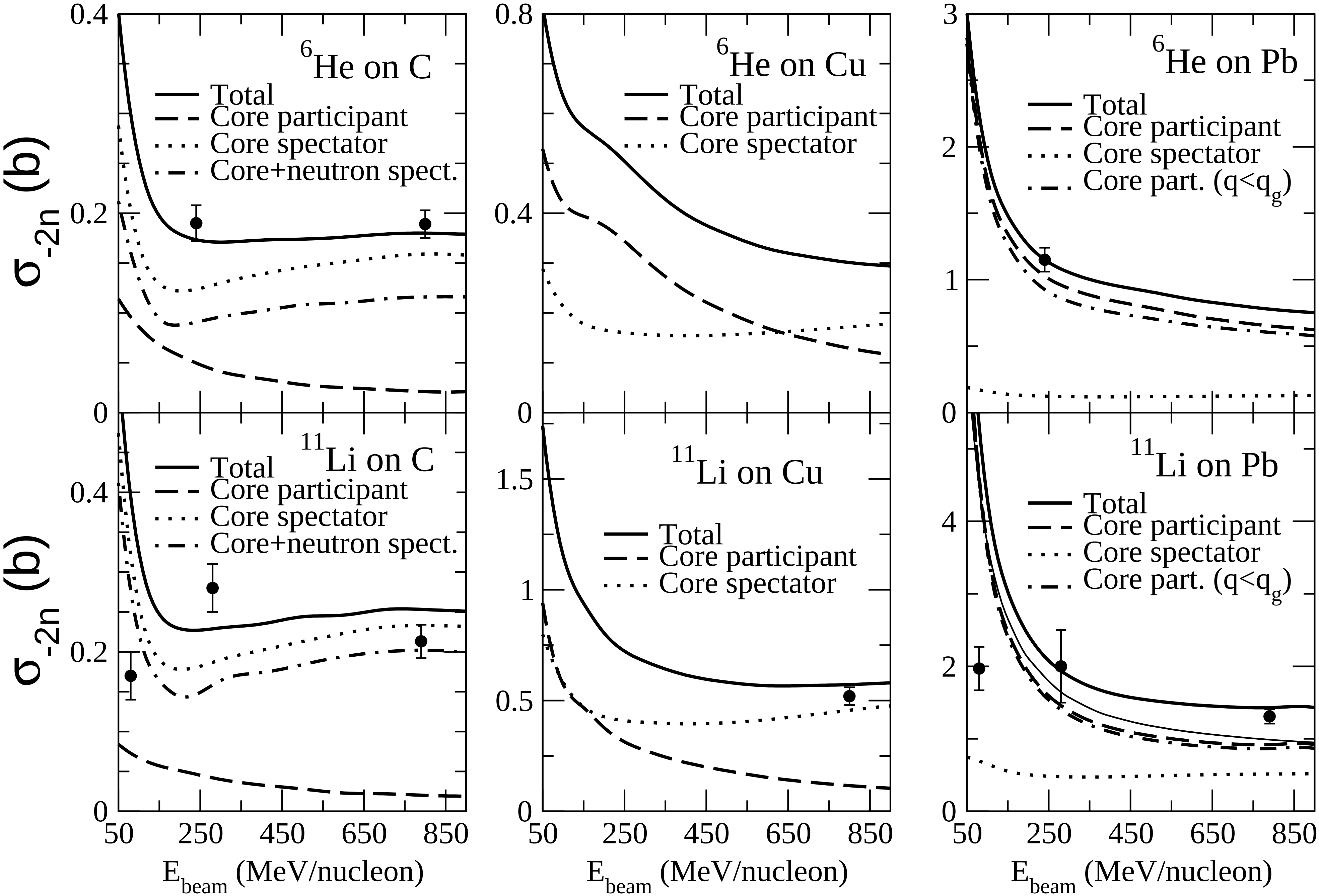

^{6}He on C
^{6}He on Cu
^{6}He on Pb
^{11}Li on C
^{11}Li on Cu
^{11}Li on Pb
Total
Core participant
Core spectator
Core+neutron spect.
Core part. ($q<q_g$)
σ_{-2n} (b)
E_{beam} (MeV/nucleon)
0
0.2
0.4
0.8
0.5
1
1.5
2
3
4
50
250
450
650
850

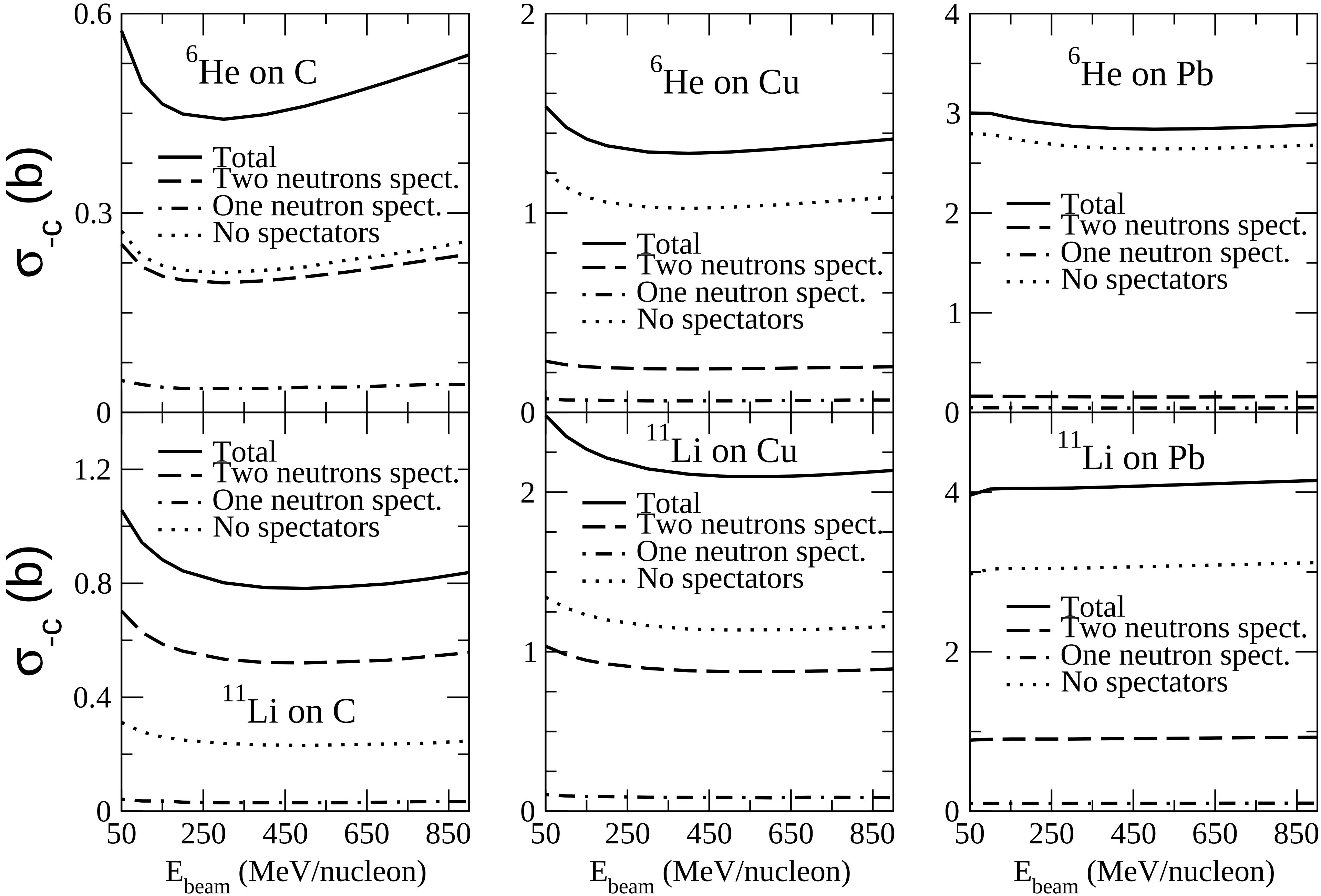

^{6}He on C
^{6}He on Cu
^{6}He on Pb
^{11}Li on C
^{11}Li on Cu
^{11}Li on Pb
Total
Two neutrons spect.
One neutron spect.
No spectators
σ_{-c} (b)
E_{beam} (MeV/nucleon)

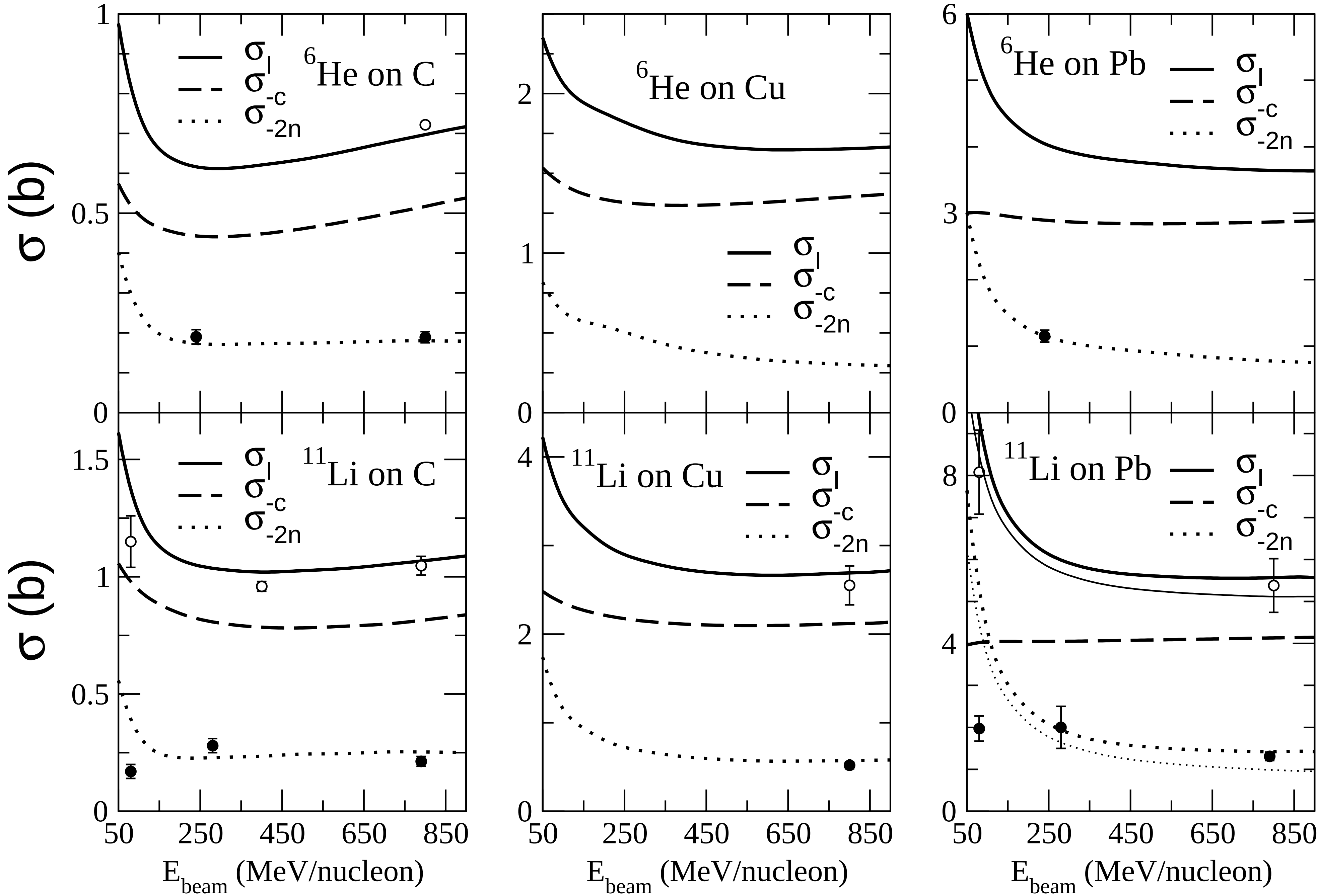

σ (b)
σ (b)
^{6}He on C
^{6}He on Cu
^{6}He on Pb
^{11}Li on C
^{11}Li on Cu
^{11}Li on Pb
σ_I
σ_{-c}
σ_{-2n}
E$_{beam}$ (MeV/nucleon)

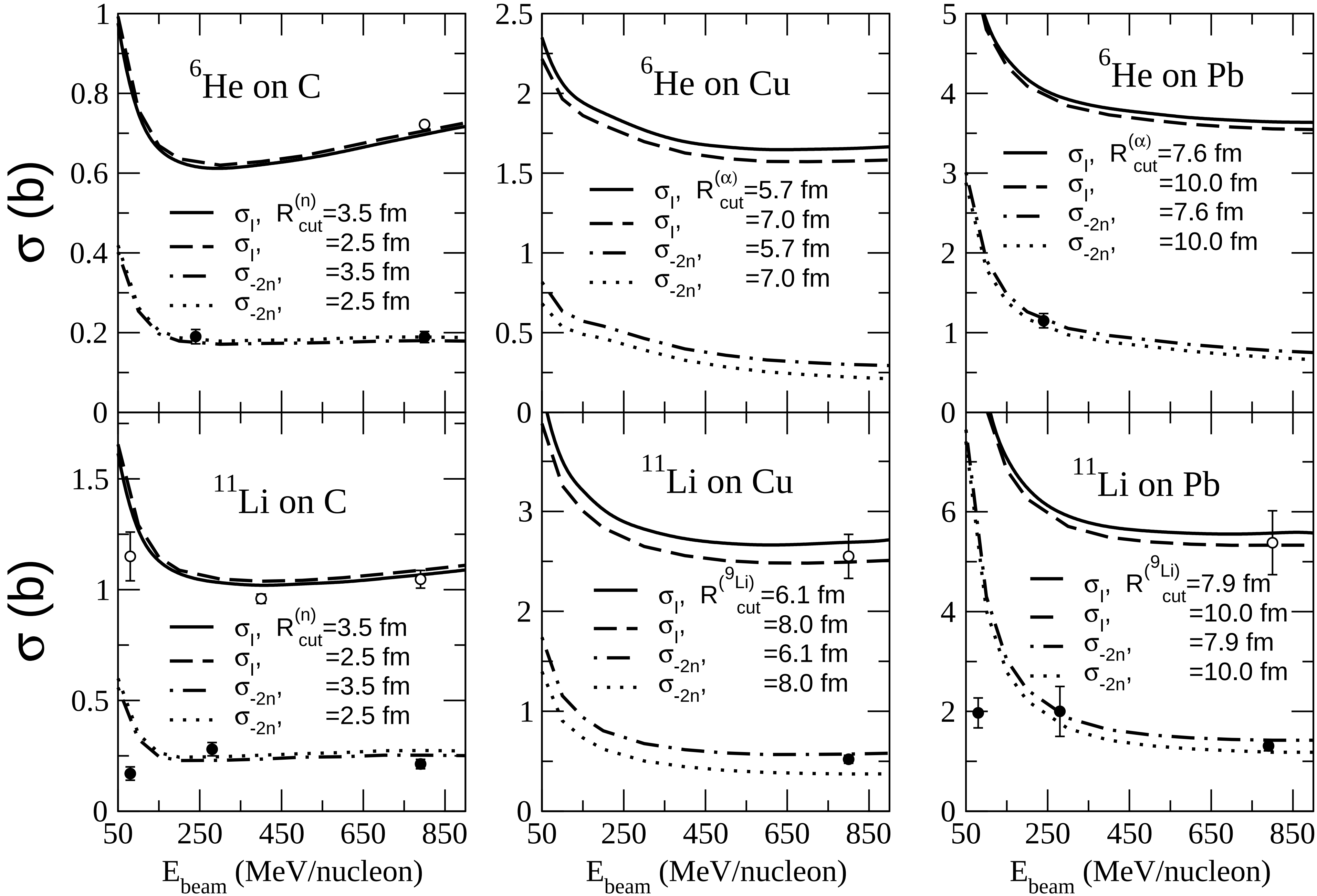

^{6}He on C
^{6}He on Cu
^{6}He on Pb
^{11}Li on C
^{11}Li on Cu
^{11}Li on Pb
σ (b)
E_{beam} (MeV/nucleon)
σ_I, $R^{(n)}_{cut}$=3.5 fm
σ_I, =2.5 fm
σ_{-2n}, =3.5 fm
σ_{-2n}, =2.5 fm
σ_I, $R^{(\alpha)}_{cut}$=5.7 fm
σ_I, =7.0 fm
σ_{-2n}, =5.7 fm
σ_{-2n}, =7.0 fm
σ_I, $R^{(\alpha)}_{cut}$=7.6 fm
σ_I, =10.0 fm
σ_{-2n}, =7.6 fm
σ_{-2n}, =10.0 fm
σ_I, $R^{(^9Li)}_{cut}$=6.1 fm
σ_I, =8.0 fm
σ_{-2n}, =6.1 fm
σ_{-2n}, =8.0 fm
σ_I, $R^{(^9Li)}_{cut}$=7.9 fm
σ_I, =10.0 fm
σ_{-2n}, =7.9 fm
σ_{-2n}, =10.0 fm

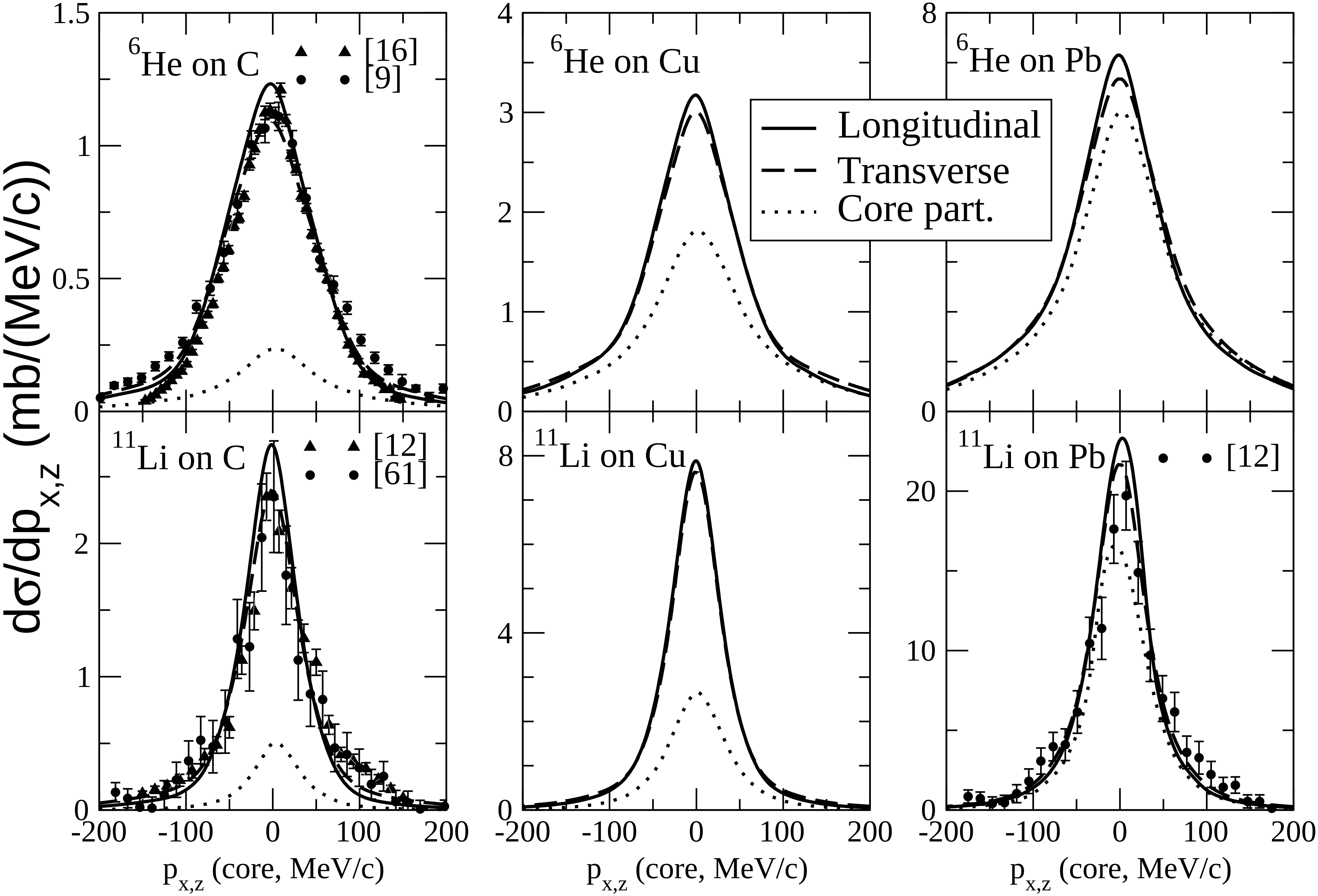

dσ/dp_{x,z} (mb/(MeV/c))
6He on C
[16]
[9]
6He on Cu
6He on Pb
Longitudinal
Transverse
Core part.
11Li on C
[12]
[61]
11Li on Cu
11Li on Pb
[12]
p_{x,z} (core, MeV/c)
p_{x,z} (core, MeV/c)
p_{x,z} (core, MeV/c)

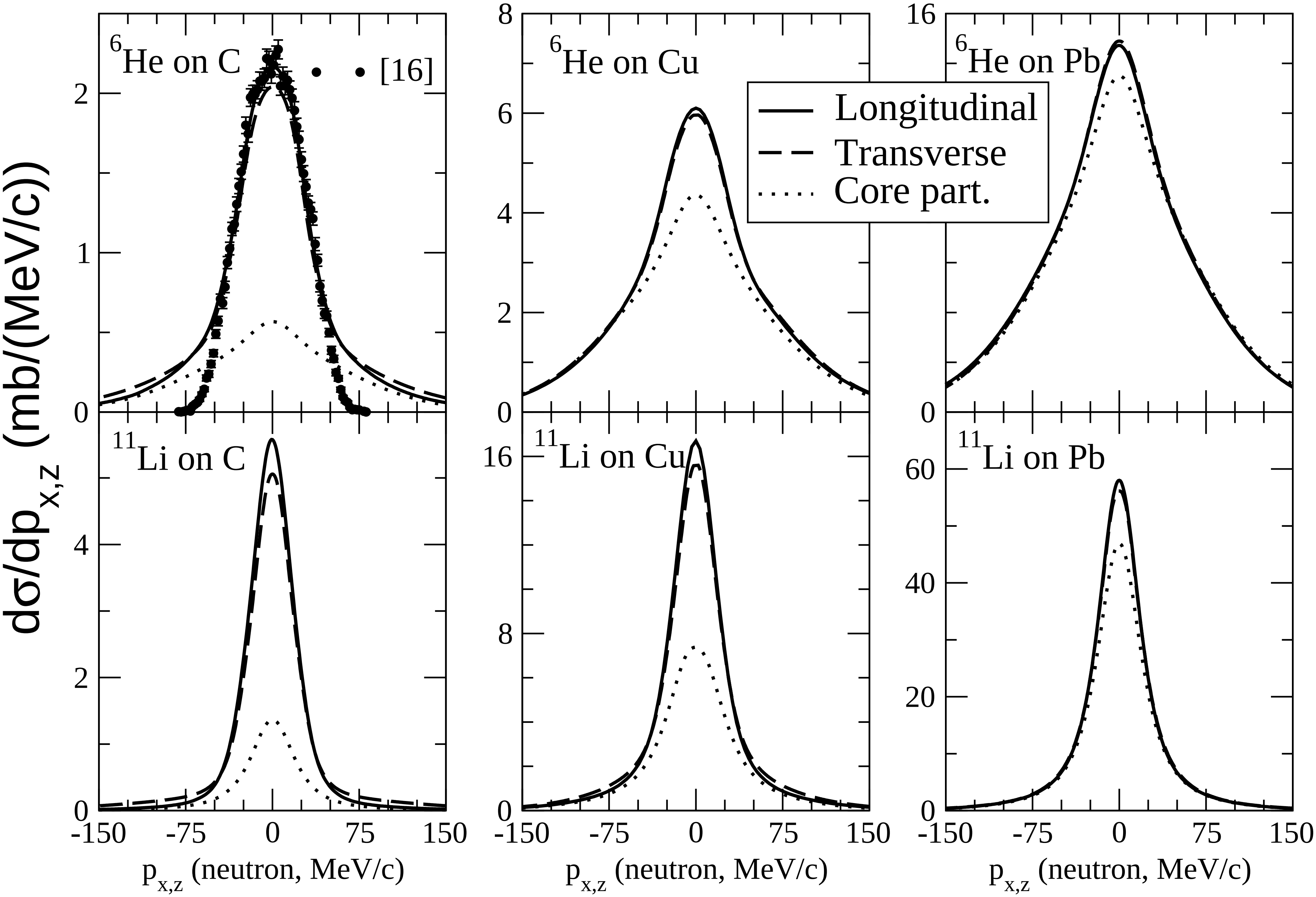

dσ/dp_{x,z} (mb/(MeV/c))
6He on C
• [16]
6He on Cu
6He on Pb
Longitudinal
Transverse
Core part.
11Li on C
11Li on Cu
11Li on Pb
p_{x,z} (neutron, MeV/c)
p_{x,z} (neutron, MeV/c)
p_{x,z} (neutron, MeV/c)

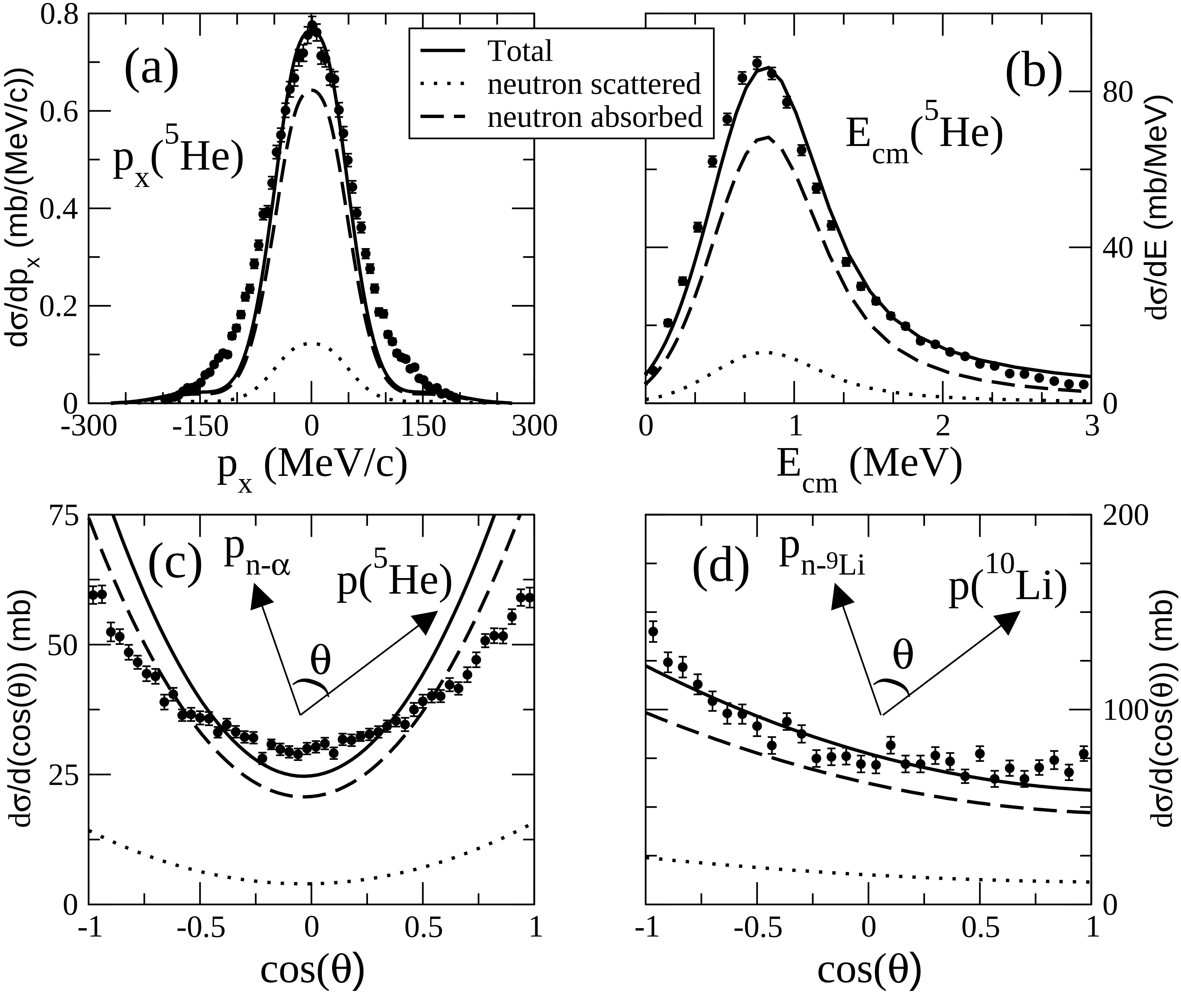

(a)
$p_x(^5He)$
$d\sigma/dp_x$ (mb/(MeV/c))
p_x (MeV/c)
Total
neutron scattered
neutron absorbed
(b)
$E_{cm}(^5He)$
$d\sigma/dE$ (mb/MeV)
E_{cm} (MeV)
(c)
$p_{n\text{-}\alpha}$
$p(^5He)$
θ
$d\sigma/d(\cos(\theta))$ (mb)
cos(θ)
(d)
$p_{n\text{-}^9Li}$
$p(^{10}Li)$
θ
$d\sigma/d(\cos(\theta))$ (mb)
cos(θ)